

# An innovative method for determining hydrological calibration parameters for the WRF-Hydro model in arid regions

M. Silver <sup>a,\*</sup>, A. Karnieli <sup>a</sup>, H. Ginat <sup>c</sup>, E. Meiri <sup>c</sup>, E. Fredj <sup>b,\*\*</sup>

<sup>a</sup> The Jacob Blaustein Institutes for Desert Research, Ben-Gurion University of the Negev, Sede Boker Campus, 8499000, Israel

<sup>b</sup> Lev Academic Center, Havaad Haleumi 21 St., Givat Mordechai, Jerusalem, Israel

<sup>c</sup> Dead Sea and Arava Science Center, Tamar Regional Council, 86910, Israel



## ARTICLE INFO

### Article history:

Received 6 July 2016

Received in revised form

12 January 2017

Accepted 12 January 2017

### Keywords:

Hydrology

Flood forecasting

Calibration

Landsat classification

GIS

## ABSTRACT

The techniques presented herein allow to directly determine certain crucial calibration parameters for the WRF-Hydro flood forecasting model. Typically, calibrations are chosen by an iterative, empirical, trial and error procedure. We suggest a more systematic methodology to arrive at a usable calibration. Our method is based on physical soil properties and does not depend on observed runoff from certain basins during specific storm events. Three specific calibration variables that most strongly affect the runoff predictions are addressed: topographic slope, saturated hydraulic conductivity, and infiltration. We outline a procedure for creating spatially distributed values for each of the three variables. Simulation runs are performed covering several storm events with calculated calibrations, with default values, and with an expert calibration. We show that our calibration, derived solely from soil physical properties, achieves forecast skill better than the default calibration and at least as good as an expert based calibration.

© 2017 Elsevier Ltd. All rights reserved.

## 1. Introduction

### 1.1. Background

Properly calibrated hydrological models can predict runoff rates and intensities with reasonable accuracy (Givati et al., 2012; Pennelly et al., 2014; Yucel et al., 2015)), thus aiding drainage authority personnel to prevent damages. Over the past decade, damage due to flooding has gained increasing attention (Foody et al., 2004; Gheith and Sultan, 2002) with the focus on forecasting as a mean to mitigate those damages. Recently integrated modeling and display frameworks have been reported (Fredj et al., 2015; Akbar et al., 2013). These systems publish forecast and model outputs in a fashion easily understood by laymen, on publicly accessible web sites. Thus early warning systems, based on calibrated forecasting models are being adopted to save lives and property damage. However the calibration process usually

continues for years, with many iterations of parameters being applied to certain storm events in certain basins, and with many simulation reruns to find the optimal calibration values.

The current research attempts to substantially shorten the calibration process and improve the spatial resolution for three calibration parameters that most influence the runoff forecasts from the WRF-Hydro model: slope, hydraulic conductivity and infiltration. Unlike earlier calibration procedures, we attempt to determine spatially distributed parameter values using physical soil and terrain properties, without requiring repeated trial and error attempts and without focusing on flood events in a particular basin.

We employ several Geographic Information System (GIS) analyses to arrive at highly detailed datasets for the three parameters SLOPECAT, REFDK and REFKDF (referring to topographic slope, saturated hydraulic conductivity, and infiltration, respectively) specifically in arid regions. These raster layers, after conversion to NetCDF format, are merged into the Land Surface Model (LSM), a collection of spatial variables such as topography, land cover, albedo, soil moisture, all of which take part in solving the hydro-meteorological energy balance equation. Then simulations are run over several storm events, focusing on certain basins, using three calibrations: the WRF-Hydro default, an expert calibration and these calculated calibration values. Resulting forecast outputs

\* Corresponding author.

\*\* Corresponding author.

E-mail addresses: [micha@arava.co.il](mailto:micha@arava.co.il) (M. Silver), [karnieli@bgu.ac.il](mailto:karnieli@bgu.ac.il) (A. Karnieli), [hananginat@adsc.org](mailto:hananginat@adsc.org) (H. Ginat), [eranmeiri@yahoo.com](mailto:eranmeiri@yahoo.com) (E. Meiri), [\(E. Fredj\).](mailto:fredj@jct.ac.il)

are compared with observed runoff from hydrometric stations at the outlets of the basins under investigation.

## 1.2. The WRF-Hydro model

The WRF-Hydro hydro-meteorological model, built and developed by the National Center for Atmospheric Research (NCAR) under the Research Applications Laboratory (RAL) over the last decade, expands the capabilities of the base WRF meteorological forecasting system. WRF implements a mesoscale Numeric Weather Prediction (NWP) model. WRF-Hydro encompasses the additional capabilities to input high resolution topographic and hydrological data, known as the terrain routing grid. This capability is described in Gochis et al. (2013), and Chen et al. (2008) present the original work on merging terrain routing layers with the LSM. Fig. 1 presents a flow diagram depicting the transfer of input and output from the initial stages through completion of the simulation.

Kumar et al. (2008) report a full Land Information System integrated with WRF-Hydro. The Hydro component then simulates surface runoff, groundwater flow and channel routing while shifting between the low resolution WRF domain and the higher resolution terrain routing grid.

Assimilation of the routing grid, and the aggregation/disaggregation of the high resolution data allow the WRF-Hydro module to integrate meteorological input data with hydrological configurations to create predicted storm hydrographs for each separate basin. Therefore this hydro-meteorological model improves on previous empirical and physical models by coupling climate forecast data, such as are available from Global Forecast System (GFS) or European Centre for Medium-Range Weather Forecasts (ECMWF), together with local topographic and geomorphological information to produce a time series of predicted runoffs.

This work presents a new method to address certain soil and topography parameters that affect the outcome of the model. Referring to Fig. 1, the geo\_em LSM calibration file is initialized at the preprocessing stage, the three hydrological parameters are merged into the LSM, then these parameters are ingested by both the WRF and Hydro stages. In the Results and Discussion (Section 3) we present a comparison of forecasts using our calculated calibrations with those based on default calibrations.

## 1.3. Model calibration

Like any environmental prediction model, WRF and WRF-Hydro require calibration in order to attain results that approach observed data. Both WRF and the Hydro component offer a large range of parameters and switches that affect the operation and outputs of the models. We diverge from the default calibration setup by calculating and incorporating the three specific hydrological parameters mentioned above.

### 1.3.1. Calibration overview

WRF and WRF-Hydro are structured to read 12 files containing tables of values for certain configuration parameters, and four "namelist" files which encompass several hundred calibration parameters. Three of the "table" files that influence the Hydro component are the SOILPARM.TBL, CHANPARM.TBL and GEN-PARM.TBL. The first consists of tables of soil parameters such as saturated water content, wilting point water content, matric pressure ( $\psi_{sat}$ ) and so on for several standard types of soils. The second defines a set of standard channel profiles and Manning coefficients that are used when the model switches from surface flow to channel flow. The GENPARM.TBL file holds default, scalar values for soil hydraulic properties including the calibration parameters that

are addressed in this research: SLOPECAT, REFDK and REFKDT. In the absence of any other spatially distributed input data for these parameters, the model simply applies the single values from this file homogeneously to the whole extent of the domain.

Among the namelist files is namelist.wps. The preprocessor system, WPS, extracts details from this file that determine the nested domain structure (see Section 2.7.1) to perform downscaling of the global atmospheric data to the size and resolution of the outer analysis domain. The WRF process itself parses namelist.input for definitions of the time step, forecast period, which micro-physics model is used.

Crucial to the Hydro component is the hydro.namelist file that lists parameters that point to the input LSM and high resolution terrain routing datasets. This namelist file also contains a set of Boolean and numeric values such as CHANRTSWCRT to activate channel routing, and AGGFACRT that contains the ratio between the high resolution terrain routing grid and the land surface model at the coarser domain resolution.

### 1.3.2. Spatial calibration parameters

In addition to the above parameters, most of which are single variables or tables of values applied globally to the model, WRF-Hydro also accepts gridded, spatial layers, incorporated into the LSM file geo\_em.d03.nc, that includes the parameters SLOPECAT, REFDK and REFKDT, comparable to the scalar parameters in GEN-PARM.TBL. Including these in the LSM NetCDF file allows spatially distributed calibration of soil parameters at the resolution of the WRF inner domain.

### 1.3.3. Background: past calibration efforts

Typically three categories have been used to describe calibration procedures: Shuffled Complex Evolution (SCE) (Duan et al., 1994), Parameter Estimation (PEST) (at <http://pesthomepage.org/> and employed by Gallagher and Doherty (2007)) or manual. Manual parameter calibration usually involves choosing values for a set of configuration parameters, and running a simulation. Then, based on the match between the forecast and observations, the configuration values are changed, and the simulation is rerun. Yucel et al. (2015) refer to this procedure as a step-wise approach, and point out the difficulty associated with calibrating any multi-parameter model due to interactions between the parameters. Nevertheless, they show Root Mean Square Error and Nash-Sutcliffe statistics indicating that optimum calibrations were found. The PEST software offers an automated approach to determining parameter values by using a Markov Chain Monte Carlo method to arrive at optimal sets of calibration parameters. The SCE algorithm solves an optimization equation to isolate the best set of parameters from a complex parameter surface. Parameter values are shuffled, and the optimization reapplied until a best combination is obtained.

Recently other efforts have been made to automate the calibration process. For example Biondi and De Luca (2015) present an assessment of parameters for flood prediction models in ungauged basins, by creating a basin signature composed of the first three L-moments of annual maxima discharge distributions. This signature is then conditioned using Monte Carlo simulations and regionalized to produce distributions of calibration parameters. However, they first discuss the difficulties associated with parameter estimation and flood forecasting in ungauged basins, and they point out the weaknesses of transferring calibrations from a nearby, gauged basin to an unknown region. Some researchers (for example Yucel et al.) nevertheless report successful transfer of calibrations from gauged to ungauged basins.

Chen et al. (2016) discuss optimization of parameters in Physical Based Hydrological Models by employing a Particle Swarm Optimization (PSO) technique. This algorithm creates sets, referred to as

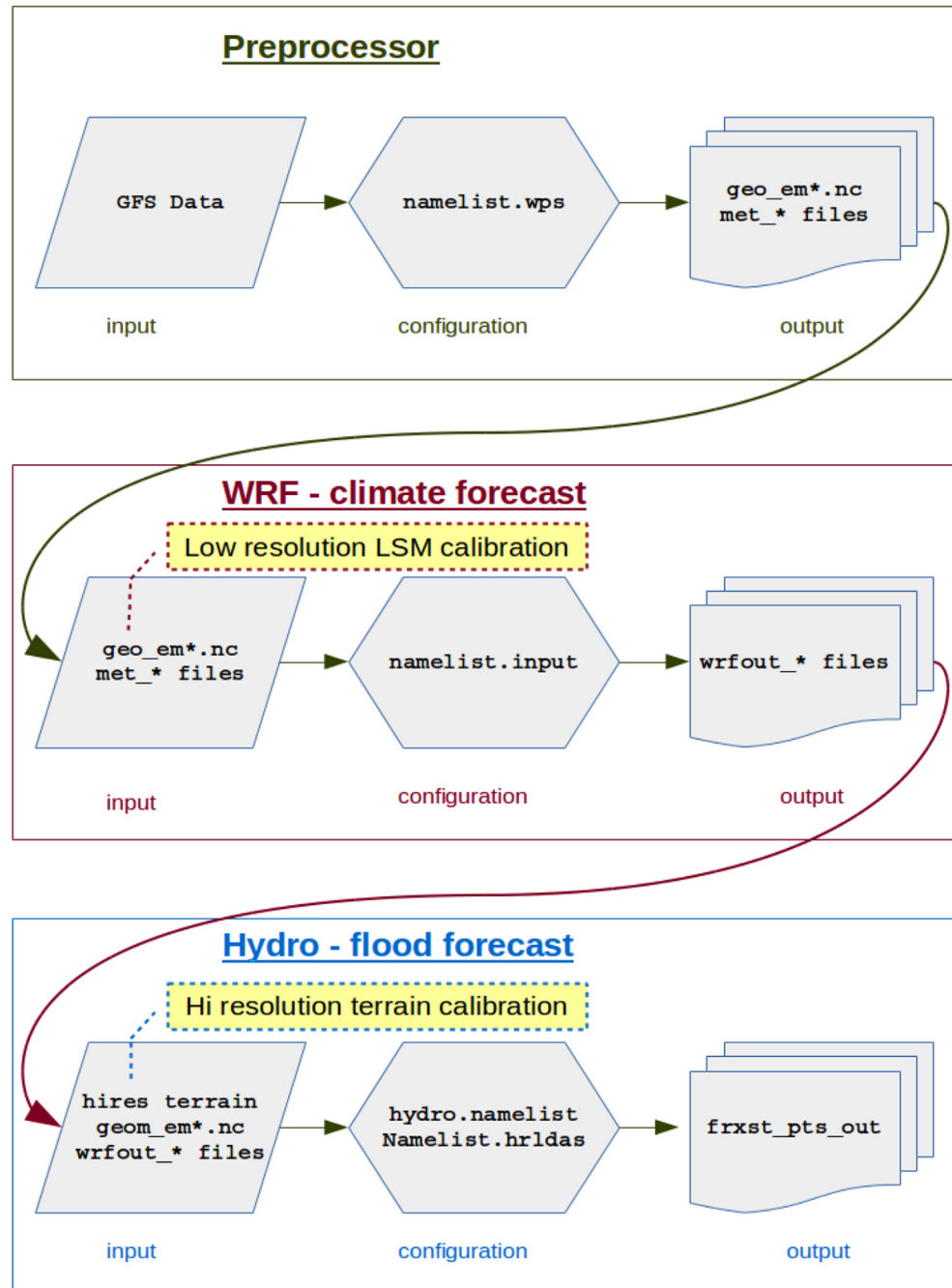


**Fig. 1.** The flow of input and output data files from the WPS stage through WRF and the final hydrological forecast. The dashed frames indicate NetCDF calibration files.

"swarms", of candidate parameters and applies equations to allow the parameter values for each of the swarms to move and evolve through the parameter domain, until an optimal solution is found. They found that with their chosen initial parameter values the PSO procedure did converge to a set of calibrations. Their work further validated the PSO results using a Liuxihe model to simulate runoff in their study area. While this work extends well beyond the typical, naive, trial and error approach, Chen et al. clearly explain the requirement for repetitive iterations of simulation runs, and comparison to measured runoff.

The cyclic procedure described above appears in other research (Hogue et al., 2000; Yilmaz et al., 2008). All these methods must overcome the same temporal and spatial shortcomings:

1. Resulting calibrations in one basin may not be suitable in another basin
2. Resulting calibrations from one series of storm events may not be suitable for other events
3. Methods are applicable only where there are observed runoff data.
4. Many repeated iterations require a long preparation time

#### 1.3.4. Calculated calibrations

The current work suggests a method to derive distributed soil parameters from satellite imagery, and then applies those parameters to the model calibration. The procedure presented overcomes

the shortcomings listed above. The method does not depend on any single basin or storm event. Furthermore, it is applicable in any arid region, where satellite imagery offers a view of bare soil, and calibration results can be obtained quite quickly. Nourani et al. (2015) show a similar approach, however they look only at NDVI to determine land use changes. Also Ohana-Levi et al. (2015) employ remote sensing to model basin runoff by assessing land use changes over a period of two decades. Their work classifies Landsat images into six landuse classes, whereas we identify soil types with different hydrological characteristics.

### 1.3.5. Default calibration

Two additional sets of calibration parameters, the WRF-Hydro defaults and an expert derived set are used as the base of comparison to evaluate the forecasting skill of the calculated calibrations. Within the initial installation of the WRF-Hydro model, one of the tables of parameters, GENPARM.TBL contains the following default values: REFDK =  $2 \times 10^{-6}$  and REFKDT = 3.0. In addition, the standard pre-processing procedure when setting up the model environment includes running the geogrid.exe (further details in 2.6) utility to create the LSM NetCDF files geo\_em.d0\*.nc. Each of these contains the SLOPECAT variable, determined by default to be 6.

## 1.4. Objectives

This work will outline a procedure based on physical soil and topography properties to determine three spatially distributed calibration parameters. After departing from the usual iterative, trial and error approach, we will derive values for the necessary parameters using GIS and remote sensing procedures combined with known soil hydrological attributes. Our method will not rely on observed runoff from particular storm events, nor from particular basins. However data from a few well forecasted storm events will be used to extract the soil infiltration factor. The method will determine calibration parameters quickly for any arid region where satellite imagery of bare soil is available.

## 2. Methodology

### 2.1. Study area and storm events

#### 2.1.1. Geographic distribution of basins

The scope of this work covers seven basins in arid and semi-arid regions of Israel and Jordan. All these basins drain into the Dead Sea, eventually. The northern most, Wadi Faria, discharges into the Jordan river north of the Dead Sea. Wadi Arugot and the smaller Darga and Kidron flow directly into the Dead Sea from the west. Tzihor, a small basin in the central Negev, empties into the large Faran watershed. Faran, the largest by far, with headwaters that extend well into the Sinai, flows north-east through the Arava valley. One basin, Uba, is located wholly in Jordan and runs north-westward draining into the Arava valley. The drainage area of each

**Table 1**  
Drainage area of basins.

Basin	Area (sq.km.)
Faria	330
Darga	78
Arugot	235
Uba	115
Tzihor	150
Faran	3340
Kidron	123

basin appears in Table 1, and Fig. 2 shows the basins on a map of the region.

Two considerations dictated the choice of these basins: all are located in arid and semi-arid regions with very low or no vegetation cover, and there are active hydrometric stations in each recording observed runoff with historical data for some years.

### 2.1.2. Storm events

After completing the calibration stage, simulations were run for the above basins, covering six storm events: March 2014, May 2014, November 2014, January 2015, February 2015 and October 2015. During each of these events rainfall occurred in parts of the country and brought flooding and damages. Preferably earlier events would also have been examined, such as January 2010 (especially in the Zihor basin) and the major storm of January 2013. However live GFS forecast climate data at 0.25° pixel size are available only for the past two years (see Section 2.7.4). Earlier GFS datasets can be ordered from offline storage, but only at higher resolutions. Thus, this work was limited to the 2014–2015 seasons.

The below details were collated from seasonal reports published by the Israeli Meteorological Service at <http://www.ims.gov.il/IMS/CLIMATE/ClimateSummary/2013/>

- During March 2014, from 8/03/2014–11/03/2014 substantial rain fell across the Negev and eastern Judean mountains, and caused runoff in the Darga and Faran basins.
- November 2014 saw record quantities of rainfall along the coastal plain and central mountains, but most of the south remained dry. However the weather front on 17/11/2014 shifted somewhat eastward towards the Dead Sea and brought runoff in Wadi Darga.
- Rainfall in January 2015 extended more or less through the whole month, bringing total precipitation to well over the monthly average in most regions of the country, and snow in the northern mountains. The Negev and Dead Sea areas, however, received less than 20 mm, just enough to cause a flood in the Darga and Arugot basins.
- The February 2015 event, beginning on 20/02/2015, again left snow accumulated in the northern mountains. We examine the Arugot, Faran and Darga basins during this event.
- The October 2015 storm from 25 to 27/10/2015 resulted in extensive flooding throughout the south, including damage to the Evrona border crossing near Eilat, and some runoff in the Faran basin.

Choice of these storm events resulted from an examination of the available recorded runoff data. Only those storms for which observed runoff was substantial at the hydrometric stations in each of the above basins were chosen.

### 2.2. GIS data and procedures

The methods outlined below rely on three base GIS datasets: elevation data from the SRTM program (Ramirez, 0000) downloaded from <http://earthexplorer.usgs.gov>; Landsat 8 OLI tiles covering the WRF domain, obtained from the same source; and a vector layer of geological soil types within Israel, obtained from the Geological Survey of Israel. The SRTM based Digital Elevation Model (DEM) raster is at one arc second resolution (approximately 30 m) and the Landsat imagery is also supplied at 30 m spatial resolution.

We used GRASS-GIS (GRASS Development Team, 2015) to perform all GIS processing in this work. This open source software, developed since 1982, has gained acceptance recently especially in academic research (as in (Neteler et al., 2012; Garcia, 2004; Gebbert and Pebesma, 2014; Grohmann et al., 2011)).

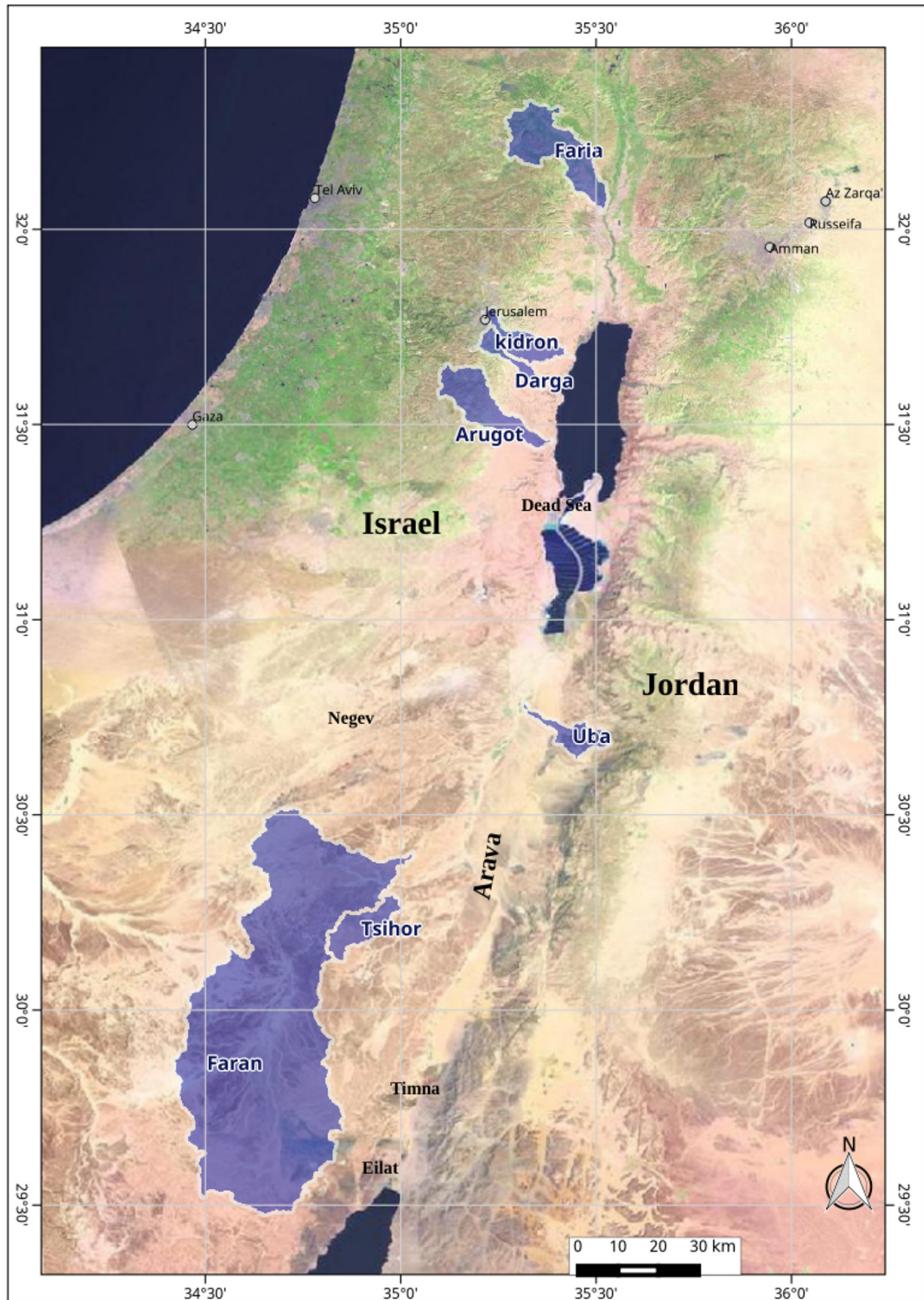


Fig. 2. Location map and studied Basins.

A supervised classification of Landsat 8 Operational Land Imagery (OLI) imagery (details appear in section 2.2.4) produced a spatial dataset of soil types covering the whole WRF domain. The training areas for supervised classification were extracted from lithology data supplied as a polygon layer by the Geological Survey of Israel. Before classification, the imagery underwent atmospheric correction (described further in section 2.2.2) in order to improve spectral response curves. Then known and published values for soil saturated hydraulic conductivity were applied to each of the features in the resulting GIS layer of soil types. This GIS layer became, after transforming to NetCDF format, the REFDK parameter used by the model.

Surface runoff is calculated within the WRF-Hydro model using a Simple Water Balance Model (SWB) formula, described by Schaake et al. (1996). This runoff equation takes into account several variables: precipitation rate, soil moisture ( $\theta_{sat}$ ) and depth. Then the SWB equation uses two parameters: saturated hydraulic conductivity ( $K_{sat}$ ) referred to as REFDK, and an infiltration coefficient ( $k_{dt}$ ), or REFKDT, to calculate surface runoff per pixel. We used this equation in the opposite sense of its purpose in the model. The infiltration coefficient was obtained by inserting observed and predicted values for runoff, soil moisture and estimates of saturated hydraulic conductivity. A function  $f(k)$  was defined as the square of the difference between observed and predicted runoffs, then the Brendt method was used to solve for values for  $k_{dt}$  when the function is at a minimum (See 2.5).

Finally a GIS process extracted the dominant slope category for each domain pixel, thus creating the SLOPECAT parameter.

### 2.2.1. Elevation data

Eight SRTM tiles were downloaded and merged into one continuous raster. The merged DEM, with water surfaces set to null served four purposes:

- elevation dataset to delineate the basins under investigation
- altitude data in the atmospheric correction procedure
- base data for producing most of the land surface model layers
- elevation data for calculating slopes to create the SLOPECAT parameter

### 2.2.2. Satellite imagery atmospheric correction

Three Landsat 8 OLI tiles were obtained from the EarthExplorer website (cited above) and then corrected for atmospheric effects. Path 174 and rows 37, 38, 39 covered southern Lebanon, all of Israel, and the eastern Sinai and southern Jordan. These data are supplied in the UTM 36N coordinate reference system. The acquisition date, August 2014, insured that cloud cover was almost zero on that date. Furthermore, by selecting the summer, dry season the imagery had minimum vegetation cover, thus allowing the best separation and classification of soil types.

This analysis used six bands: red, green, blue, Near Infrared (NIR), Shortwave Infrared (SWIR) SWIR-1, and SWIR-2. The Aeronet website: <http://aeronet.gsfc.nasa.gov/> publishes values for Aerosol Optical Density (AOD) at the approximate acquisition time of the Landsat imagery, for wavelengths of 500 and 675 nm. The Aeronet site also provides atmosphere water content. Interpolating between values gives an estimated AOD at the correct acquisition time, and at 550 nm. These AOD and water content values were entered into the web interface for 6S: <http://www-loa.univ-lille1.fr/Wsixs/> to produce the set of configurations for the 6S algorithm.

Next Top of Atmosphere (TOA) reflectance was calculated using the metadata in the Landsat Metadata (MTL) file. Finally the 6S procedure, incorporated into GRASS-GIS, produced atmosphere corrected raster layers for each of the six bands. A comparison of

atmospheric correction strategies, performed by Raab et al. (2015), shows equivalent results for several software implementations, among them GRASS-GIS. This module also reads as input the DEM, described above, to properly account for elevation and atmosphere thickness. The following step 2.2.4, used all six bands, and spectral response curves for all the bands showed improved contrast after atmospheric correction.

### 2.2.3. Lithology

The layer of soils throughout Israel, from the Geological Survey of Israel, contained 109 separate lithology categories. Several appeared only in the north, and were ignored. Other categories covered very small, negligible areas. The full set of soil types was distilled to 26 categories, from which a set of training polygons was selected and used in the following Section 2.2.4.

### 2.2.4. Classification of satellite imagery

The catchment areas of several large basins in the southern Negev region of Israel drain areas from both Egypt and Jordan. Notably, almost half of the 3300 square kilometer Faran basin lies in the Sinai. Several basins draining the western slopes of the Jordanian hills cause damage to settlements in the Arava valley. In order to characterize runoff from these basins, soil hydraulic parameters need to be determined for these areas outside the border of Israel. Therefore a supervised classification of satellite images provided the means to estimate soil types with remote sensing throughout the full WRF-Hydro domain, covering areas beyond the border of Israel.

The method used here is somewhat similar to land use classification as presented by Rozenstein and Karnieli (2011). However we manually prepared training area polygons, without the need for a preparatory unsupervised classification. Instead training areas were extracted from lithology spatial data, supplied by the Geological Survey of Israel, (which are limited to the border of the country). Fig. 3 shows the training polygons.

In addition to the lithology data, three additional categories were defined to account for water surfaces, urban areas, and forests or agricultural fields. The remote sensing classification procedure easily distinguishes spectral signatures from pixels in each of these non-soil areas. Since the hydrological behavior of surface flow in each is unique and not necessarily dependent on soil type, we separated these pixels into their own categories. Water surfaces do not take part in surface flow so values for the soil calibration parameters were set to null. Urban areas should show very low infiltration (see Salvadore et al. (2015), especially their discussion of impervious cover percentage), and high runoff, so the calibration is similar to rocky areas. Regarding forested or agricultural areas we recognize that the remote sensing classification cannot contribute any information to soil hydraulic properties due to vegetation cover, so values in pixels classified as forest are left at the default. Since this work focuses on arid region basins, the forested and vegetation areas did not play a part in runoff predictions for the basins under investigation.

Using these training areas, the image classification procedure produced a soil lithology layer (with water, urban and forested areas also identified) that covers all of Israel as well as regions in Egypt and Jordan that drain into basins in Israel. We chose the Sequential Maximum a Priori (SMAP) method of supervised classification. McCauley et al. (1995) compare three classification algorithms and demonstrate that SMAP results in less "salt and pepper" effect, and more contiguous areas.

Several categories in the lithology data represent soils with very similar hydraulic properties. After classification, these categories were aggregated, such that only four remained, with widely varying soil properties. All sandy regions were clustered together. All

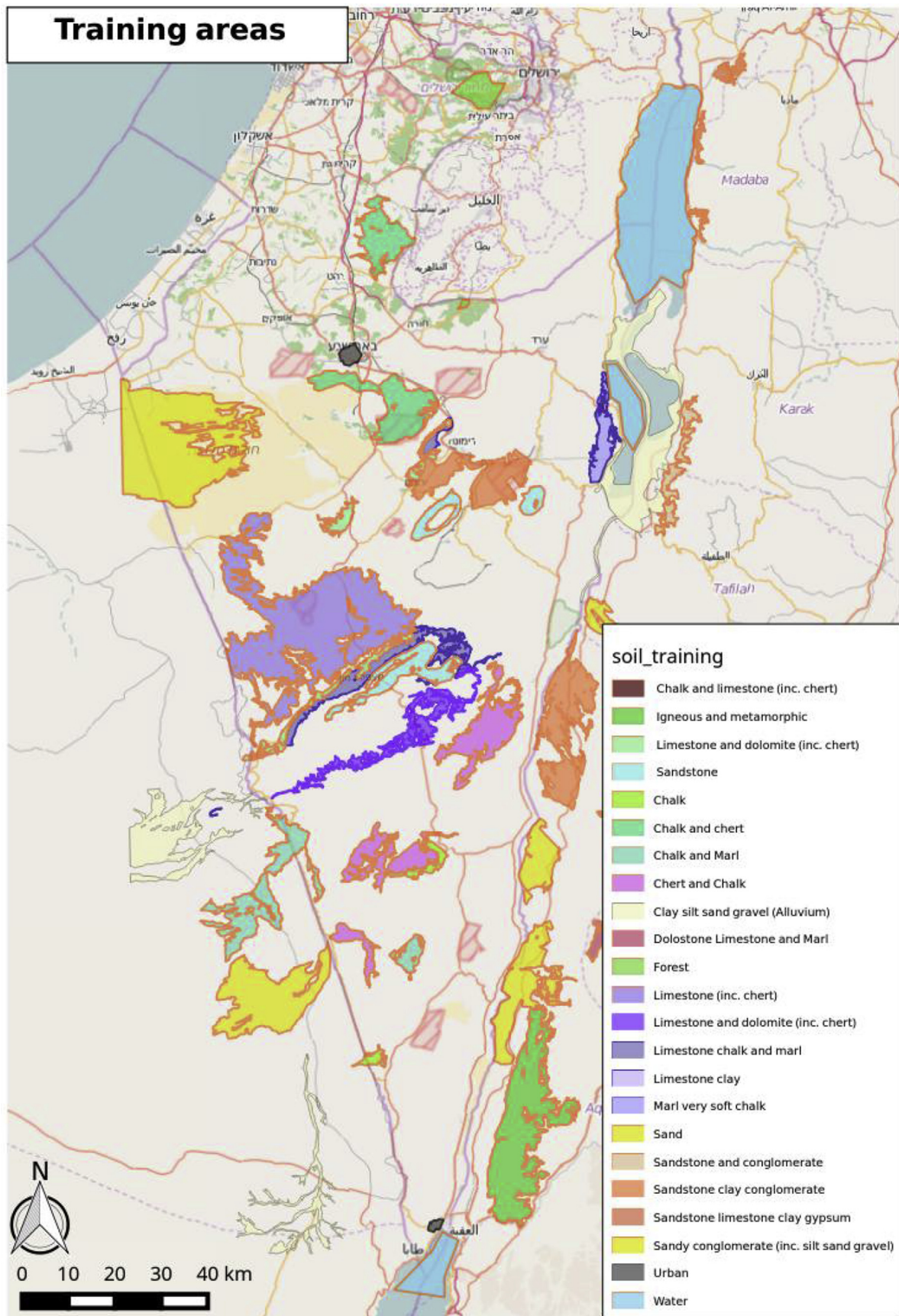


**Fig. 3.** Classification Training Polygons, as extracted from the Geological Survey of Israel lithology data.

rock regions became one classification, and so on. The assumptions behind this aggregation are explained in section 2.4. Thus the resulting soil classification map, Fig. 4 shows the four soil group categories and the three additional surface classifications, water, urban and forest.

### 2.3. Determining SLOPECAT

The SLOPECAT parameter actually influences groundwater flow, and causes only a secondary effect on surface flow. Areas exhibiting a steep slope will allow for rapid ground water drainage at the base of the soil column, and thus indirectly increase infiltration rate. After some hours this can lead to a decrease in surface flow. The parameter represents an index into an array of factors, presented in Table 2. The SLOPECAT value (at each domain pixel) is read into the model, and used to determine which factor to apply. The soil hydraulic conductivity is multiplied by that factor to estimate the rate of ground water flow. The categories represent slope classes as set down by Zobler (1986) over thirty years ago, and still published by the FAO. The first three categories are slope classes: up to 8%, from 8% to 30%, and above 30%. The next four classes consist of combinations of the first three. So an area with a mix of slopes can have SLOPECAT 4 or above. For example, a domain pixel that covers both a flat valley bottom as well as steep cliffs at the edge of the valley would have SLOPECAT 5.

While the concept of slope categories is easy to comprehend, implementing a method to create a grid of SLOPECAT values proved more challenging. The dominant slope class for each grid cell needs to be determined, allowing for the mixtures of slope classes described above. The procedure involves the following:

- The SRTM elevation data described in 2.2 served as the base layer.
- From this base layer a slope raster, with units in percent, was created.
- Map calculator expressions then extracted three raster layers for each of the first three slope classes. These data sets are Boolean values; each pixel that fits the slope class has value 1, and all other pixels are set to null.
- After switching to the coarser domain resolution of 1500 m per pixel, a GIS function summed all non-null pixels in the fine resolution DEM grid, and entered that sum into the coarse resolution grid cell. Thus three coarse resolution raster layers resulted for each of the three base slope classes with a count of the fine resolution pixels contained within the coarse domain resolution pixel.
- Finally, a specially constructed map calculator string of *if...then...else* expressions created the full SLOPECAT raster. Those pixels with a large count of fine resolution pixels for a certain class (at least 2/3 of the total size of the domain resolution cell) were given the SLOPECAT value of that class. And those with above 1/3 the total cell size from each of two classes were assigned the SLOPECAT that represents the respective combination of those two classes.

With this procedure those areas that are mostly flat were separated from areas that are moderately sloped or those that are steeply sloped. We also identified areas that have a mixture of slopes, and allocated the correct SLOPECAT to each.

### 2.4. Determining REFDK

In order to assign suitable saturated hydraulic conductivity values to each soil type, we made a simplifying assumption regarding hydraulic characteristics. All lithology types were

grouped into one of four categories: rock, reg surfaces, clay soils and sand. We chose these four groups taking into consideration the order of magnitude differences in hydraulic behavior between them. Then three sources of soil hydraulic parameters were consulted: published tables of saturated hydraulic conductivity; the set of soil parameters supplied with WRF-Hydro, and results from a Pedotransfer function (2.4.1).

Tables of estimated, average saturated hydraulic conductivity for different soils, such as are published on the USDA web site: [http://www.nrcs.usda.gov/wps/portal/nrcs/detail/soils/survey/office/ssr10/tr/?cid=nrcs144p2\\_074846](http://www.nrcs.usda.gov/wps/portal/nrcs/detail/soils/survey/office/ssr10/tr/?cid=nrcs144p2_074846) or which appear in Ritzema (1994), Chapter 12, page 16 (shown in Table 4) reaffirm the basis for the above assumption. Among the tables of values supplied as part of the WRF-Hydro setup, the file HYDRO.TBL includes a list of default saturated hydraulic conductivity values, referred to as SATDK appears for different soil types.

#### 2.4.1. Determining hydraulic conductivity using a pedotransfer function

Pedotransfer functions have proved useful and efficient in estimating soil hydraulic parameters from soil texture (Goncalves et al., 2008; Wosten et al., 2001). One implementation method, based on neural network analysis, takes as input the percentages of sand, silt and clay, as well as bulk density in a soil sample, and outputs hydraulic parameters, including saturated hydraulic conductivity. The ROSETTA software application<sup>1</sup> appeared late in the decade of 1990 (Schaap et al., 2001), and was incorporated in the Hydrus<sup>2</sup> soil flow and solute transport model.

Meiri (2015) collected a small number of soil samples from a basin in the southern Arava, separated the soil into granule sizes, and also performed a bulk density calculation. Results for the three classes of soil appear in Table 3 with  $K_{sat}$  as estimated by the neural networks procedure in Hydrus 1-D. These soil saturated hydraulic conductivity values were taken into account, together with the published  $K_{sat}$  values mentioned above when choosing the REFDK values which appear in Table 5.

#### 2.4.2. Final hydraulic conductivity values

Thus, all rocky surfaces, typically limestone or sandstone in the Negev region, were collated together and assigned a single, low value for hydraulic conductivity. Similarly a suitable, high value of  $K_{sat}$  was chosen for all sand areas, medium values for clay soils, and somewhat lower values for areas with reg surface. The reg soils in southern Israel were described thoroughly by Dan et al. (1982). Table 5 shows the selected values of REFDK (equivalent to  $K_{sat}$ ) for the different soil groups.

### 2.5. Determining REFKDT

We attempted to gain an estimation of the infiltration scaling parameter, REFKDT, by solving the WRF-Hydro model's runoff equation. The Simple Water Balance (SWB) formula, implemented within the model, solves for surface runoff as a function soil moisture, soil depth, and precipitation. The parameters in the SWB equation are soil hydraulic conductivity and an infiltration scaling factor called REFKDT. Both observed and predicted values for precipitation, soil moisture, and runoff were obtained, then an objective function was applied to solve for the  $K_{dt}$  infiltration scaling factor.

<sup>1</sup> downloadable from the USDA website.

<sup>2</sup> PC-Progress Hydrus 1-D software.

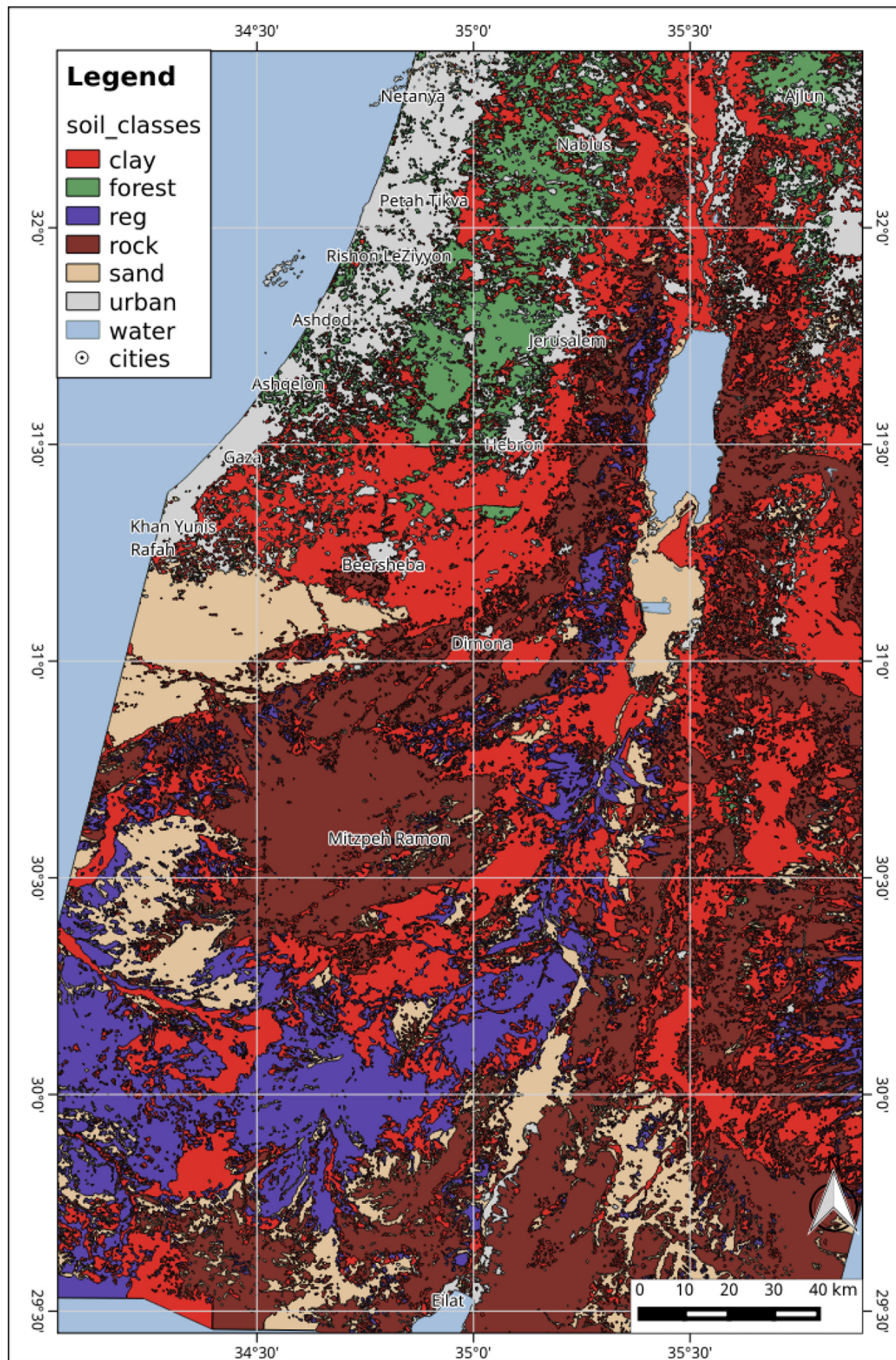


Fig. 4. Final soil classes map, after atmospheric correction of Landsat images, and SMAP classification.

**Table 2**  
Slope categories.

SLOPECAT	Slope Class (as % rise)	Factor
1	up to 8%	0.1
2	from 8% to 30%	0.6
3	above 30%	1.0
4	either category 1 or 2	0.35
5	either category 1 or 3	0.55
6	either category 2 or 3	0.8
7	any of categories 1,2,3	0.63
9	sea ice	0

**Table 3**  
Pedotransfer Function data and results.

Soil Class	Sand %	Silt %	Clay %	$\rho_b$	$K_{sat}$ m/sec
Sand	89	1.6	9.4	1.66	$17.4 \times 10^{-6}$
Reg surface	57	17	26	1.64	$1.0 \times 10^{-6}$
Colluvium	56	29	15	1.46	$3.0 \times 10^{-6}$

Data collected and analyzed by Meiri.

**Table 4**  
Range of  $K_{sat}$  values by soil texture, Ritzema (1994), Chapter 12.

Texture	K (m/day)	Min	Max
Gravelly course sand	10	50	
Medium sand	1	5	
Sandy loam, fine sand	1	3	
Loam, well structured clay loam	0.5	2	
Very fine sandy loam	0.2	0.5	
Poorly structured clay loam	0.002	0.2	
Dense clay (no cracks)		0.002	

**Table 5**  
Values for  $K_{sat}$  and  $K_{dt}$  assigned to each soil type.

Soil group	$K_{sat}$ ( $10^{-6}$ m/sec))	$K_{dt}$ (unitless)
	REFDK	REFKDT
Rock	0.5	0.8
Reg surfaces	1.5	2.0
Clay soils	2	1.8
Sand	15	4.0
Urban	1	1.0
Forest	3	3.0
Water	(set as 0)	(0)

### 2.5.1. Source of observed values for the SWB formula

The observed values were supplied by work (unpublished Master's thesis) done by Meiri and a report from earlier research on rain/runoff ratios by Greenbaum et al. (2003). Both research groups calculated rain/runoff ratios for small plots with uniform soil surfaces. The work by Greenbaum et al. utilized an artificial precipitation system of sprinklers, whereas Meiri collected runoff from plots immediately after an actual rain event. They measured rain/runoff ratios by collecting runoff in funnel shaped troughs embedded into the soil surface. The quantity of collected runoff was measured and rain/runoff ratios recorded for various soil surfaces.

Additional observed rainfall and runoff measurements were available from an ongoing field experiment in a small drainage basin ( $0.322 \text{ km}^2$ ) in the Timna valley. The soils in this wadi have been mapped (Fig. 5), and are almost all rock surfaces. The percentage area of each soil type appears in Table 6. Thus we have rain/runoff ratios from an actual, small basin with mostly uniform, rocky soil. Table 7 summarizes the data from these three sources.

### 2.5.2. Sources of predicted values for the SWB formula

We extracted predicted values for runoff and soil moisture from model simulation outputs at locations with soil similar to the types in the observations above. Soil moisture in the WRF-Hydro NetCDF output files is called SMSTOT, surface runoff SFCRNOFF, and total precipitation is obtained as the sum of RAINC and RAINNC. These variables were extracted from the WRF-Hydro output files at a chosen time slot during a storm event, and at pixel locations such that the soil type was similar to the soils in the observations.

### 2.5.3. Runoff equation

Following the explanation in Chen and Dudhia (2001) and developed by Arnault et al. (2015) (in print) we begin by expressing runoff as the difference between rainfall and infiltration:

$$R = P_d - I_{max} \quad (1)$$

where  $R$  is runoff during a time interval,  $P_d$  is rainfall, and  $I_{max}$ , infiltration, is given by

$$I_{max} = P_d * \left[ \frac{D_x(1 - e^{-k})}{P_d + D_x(1 - e^{-k})} \right] \quad (2)$$

The term  $D_x$  represents the total soil moisture content and is calculated as:

$$D_x = \sum_{i=1}^4 \Delta Z_i (\theta_{sat} - \theta_i) \quad (3)$$

where  $\theta_{sat}$  is the saturated volumetric water content,  $\theta_i$  is the volumetric water content in soil layer  $i$ , and  $\Delta Z_i$  is the depth of layer  $i$ .

The exponent  $k$  is a scaling factor that gives the REFKDT calibration value with the relation:

$$K_{dt} = k * \frac{K_{ref}}{K_{sat}} * \frac{1}{\delta} \quad (4)$$

where  $K_{sat}$  is the saturated hydraulic conductivity for each soil type (in m/sec), and  $K_{ref}$  is a constant, set within the WRF-Hydro model as  $2.0 \times 10^{-6} \text{ m/sec}$  and  $\delta = \frac{3600}{86400}$  converts from the simulation time step of 1 h to the equation time interval of 24 h.

Then we derive the runoff/precipitation ratio (labeled  $Q_r$  below) from 1 and 2:

$$Q_r = \frac{R}{P_d} = 1 - \left[ \frac{D_x * (1 - e^{-k})}{P_d + D_x * (1 - e^{-k})} \right] \quad (5)$$

### 2.5.4. Solving the runoff/precipitation ratio equation

Examining equation (5), there are constant values to insert for precipitation, and soil moisture. However, solving for  $k$  directly cannot be done since the variable appears as an exponent in both the numerator and denominator. Instead we adopted the strategy of finding an optimal solution to the square of the difference between observed and measured values. By squaring the difference we insured that the resulting function is unimodal and a single optimal solution exists for  $k$  when the function is at a minimum. Brendt's method can be applied to this function to efficiently find a close value for  $k$  when the square of difference between observed and predicted values is at a minimum.

Let  $Q_{obs}$  be runoff/rainfall values from observed experiments as described in 2.5.1, and  $R_{Pred}$ ,  $P_{Pred}$  be predicted runoff and rain rates

## Nehushtan Basin

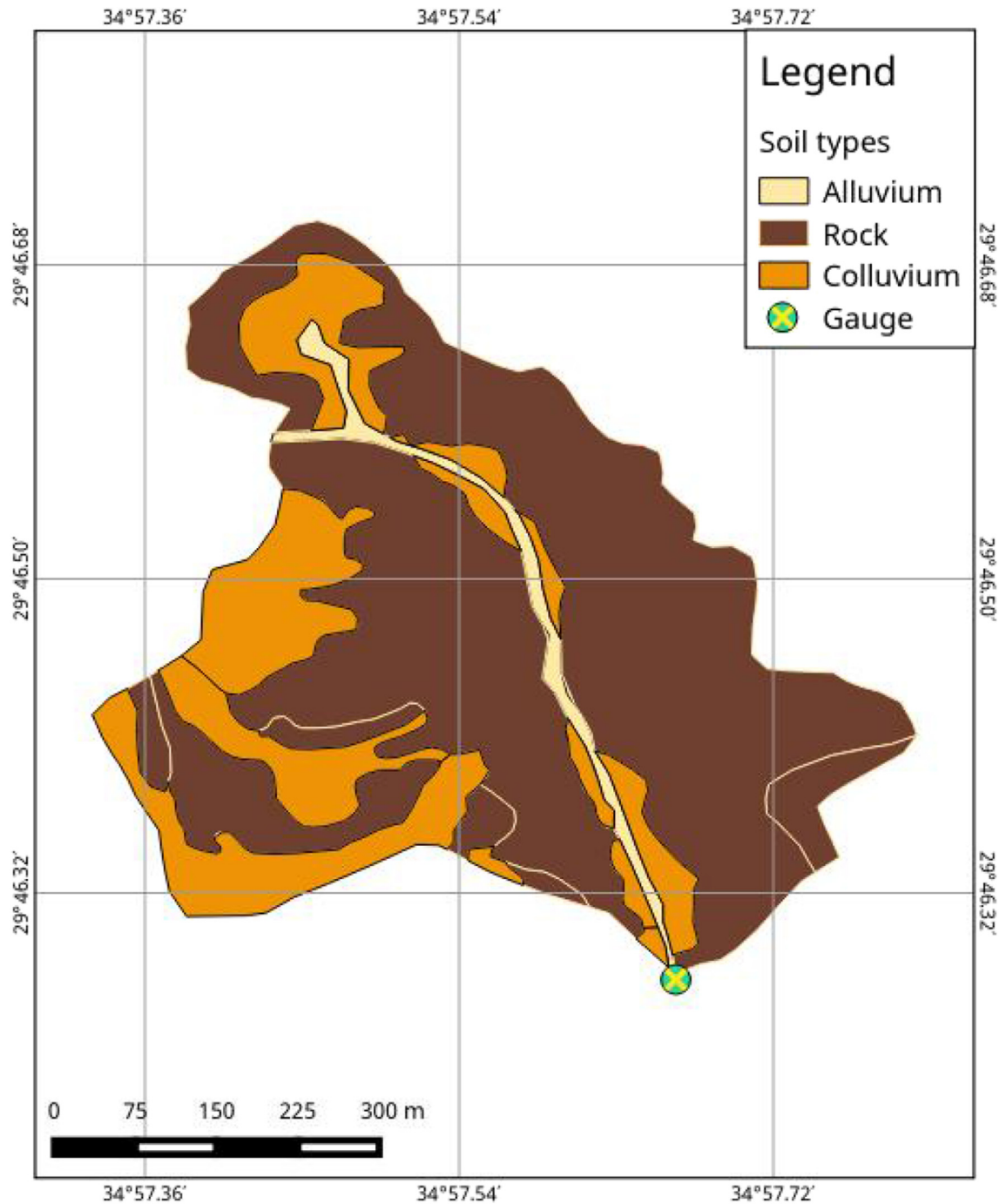


**Fig. 5.** Soil surfaces in Timna Valley basin.

from model simulations respectively.  $D_{Pred}$  represents total volumetric soil moisture in the model predictions, then the difference will be (applying equation (5)):

$$Q_{obs} - \frac{R_{Pred}}{P_{Pred}} = [Q_{obs}] - 1 + \left[ \frac{D_{Pred} * (1 - e^{-k})}{P_{Pred} + D_{Pred} * (1 - e^{-k})} \right] \quad (6)$$

The rain/runoff ratios will be constants for each soil type, as will

the soil moisture and precipitation. For readability we replace the difference between observed and predicted rain/runoff ratios with  $\mathcal{C}_{diff}$ , then squaring we define the function  $f(k)$ :

$$f(k) = [\mathcal{C}_{diff}]^2 \quad (7)$$

An approximate solution to this function, with values entered for each of the constants, is solved using an implementation of

**Table 6**

Soil surface types in the Timna Valley basin.

Soil type	Percent
Granite	61.7
Colluvium with granite	4
Terraces	4.7
Colluvium with sandstone	4.4
Sandstone	9.4
Colluvium with dolomite and sand	12.6
Alluvium	3.2

**Table 7**

Values of Precipitation, runoff/rain ratios for various soils and from various sources.

Source	Plot	Date	Soil group	Runoff/Rain		Precip. rate mm/hr.
				%	mm/hr.	
Meiri	1	Dec 2014	rock	23	26	
Meiri	5	Dec 2014	rock	70	26	
Meiri	1	Oct 2015	rock	66	97	
Meiri	2	Oct 2015	clay	49	97	
Meiri	12	Oct 2015	reg	41	97	
Greenbaum	Rocky	2003	rock	52–86	60	
Greenbaum	Colluvium	2003	sand	26–43	60	
Greenbaum	Alluvium	2003	silt	44–69	60	
Nehushtan	basin	Dec 2014	rock	7		

fminbound () which uses Brent's method to approach an optimal value for  $k$ . The method finds a value such that the square of the difference in ratios is minimum.

$$\min_{k=0.5}^{10} f(k) \quad (8)$$

Boundary values for  $K_{dt}$ , according to the WRF-Hydro recommendations, were set between 0.5 and 10. The optimal value of  $k$  was then used in equation (4) to obtain the model calibration value for REFKDT. The solutions, obtained for each soil type, appear in Table 5.

The graph in Fig. 6 shows an example output of this procedure. The curve in the graph represents the squared differences between observed and predicted rain/runoff ratios, and the large circle marker, at the curve minimum, is identified by the fminbound () function.

### 2.5.5. Constraints of the SWB equation method

We consider it important to point out two constraints when applying the SWB method to solve for values of REFKDT. The first concerns spatial extent and the second points to uncertainty in the WRF climate forecast.

In order to use equations (6) and (7) and to extract the soil REFKDT value from known surface runoff, observations at the same resolution as the model are required. In other words, observed rain and runoff data must be collected from small, uniform tributaries in a stream network. Local catchments need to be isolated that have both topography and homogeneous soil cover which will allow for installation of hydro-meteorological equipment and collection of runoff data from a uniform area. The example presented above (2.5.1) in the Timna Valley basin fits this requirement.

Furthermore, a successful optimized solution to the SWB equation requires accurate forecasts for soil moisture, precipitation and runoff. With the recognized uncertainty in WRF climate forecasts (pointed out by Fiori et al. (2014) and Hong and Lee (2009) and others) a careful examination of the synoptic state during a storm event, and comparison with the WRF forecast is required. Only after choosing a storm event that is correctly forecasted by

WRF can the model outputs be applied to obtain a reliable optimized solution to the SWB equation.

### 2.6. Preparing the calibration file

Two parallel sets of LSM files, the default and the calculated calibrations, and a third based on values from an expert calibration (from IHS) were prepared using NCO commands. Each base LSM file contains over 45 variables such as topography, albedo, landuse, soil depth, etc. Among these is also SLOPECAT. However the base install does not include REFKDT nor REFDK. In the standard WRF-Hydro version these parameters are single scalar options applied domain-wide from values in the GENPARM.TBL file.

The version of WRF-Hydro<sup>3</sup> used in this work accepts spatially distributed values for both REFDK and REFKDT, thus these variables must be added to the LSM files. We employ a python program<sup>4</sup> to add the extra variables. Then the values determined by the above procedures were inserted into the LSM files, creating spatially distributed SLOPECAT, REFDK and REFKDT parameters. Referring back to Fig. 1, the various geo\_em\*.nc NetCDF files are read into the model at both the WRF and Hydro stages.

#### 2.6.1. The default calibration

Default values for REFDK and REFKDT appear in the GENPARM.TBL parameters file. The default calibration contains uniform values throughout the domain for each of the three parameters examined in this work: REFDK =  $2.0 \times 10^{-6}$ , REFKDT = 3.0 and SLOPECAT = 6. These parameter values served as a control against which the forecasting skill of our calculated calibration was tested. A further check of the accuracy of our calibration was performed by comparing with model simulations based on an expert calibration. We rely on work done at Israel Hydrological Service (IHS) from 2013 to 2015 to calibrate an operational flood forecasting system.<sup>5</sup> The IHS parameters were inserted into a separate LSM calibration file, and simulations run using those parameters on certain flood events.

### 2.7. Simulation runs

In order to demonstrate that the method presented in this work creates a reasonable model calibration, predicted hydrographs for several storm were prepared using our calculated calibration, the WRF default, and a third expert calibration with values adopted by IHS.

#### 2.7.1. Domain setup

Both WRF and WRF-Hydro run in the framework of spatial, nested domains, where global meteorological data is downscaled to regional and then local sectors. The raw climate data used in this work was acquired from the National Centers for Environmental Prediction (NCEP) download site: <http://www.ftp.ncep.noaa.gov/data/nccf/com/gfs/prod>. NCEP distributes these GFS model climate forecasts at 0.25° pixel size that is downscaled by WPS, the WRF preprocessor, to a resolution of 13 500 m (user defined in the namelist.wps file). Thus our first, outer domain  $d01$  was constructed with 13.5 km pixels. We chose a 1:3 ratio for the middle domain  $d02$ , giving pixels of 4500 m. Then we defined inner domains, also at a ratio of 1:3 in relation to the middle domain, thus resulting in final analysis domains  $d03$  and  $d04$  of 1500 m. Figs. 7 and 8 show maps of this domain setup.

<sup>3</sup> developed by Thomas Rummel, University of Augsburg.

<sup>4</sup> also supplied by Thomas Rummel.

<sup>5</sup> obtained from personal communication with Dr. Amir Givati.

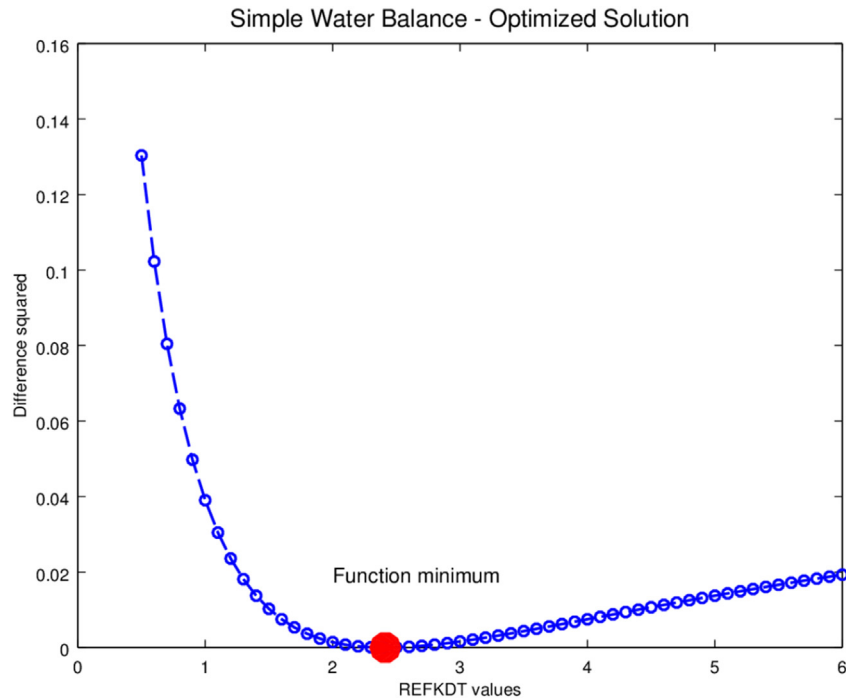


**Fig. 6.** A sample optimized solution to the SWB equation. This graph represents the squared difference between observed and predicted rain/runoff ratios for a soil of  $K_{sat} = 2 \times 10^{-6} m/sec$  with observed rain/runoff ratio of 0.6.

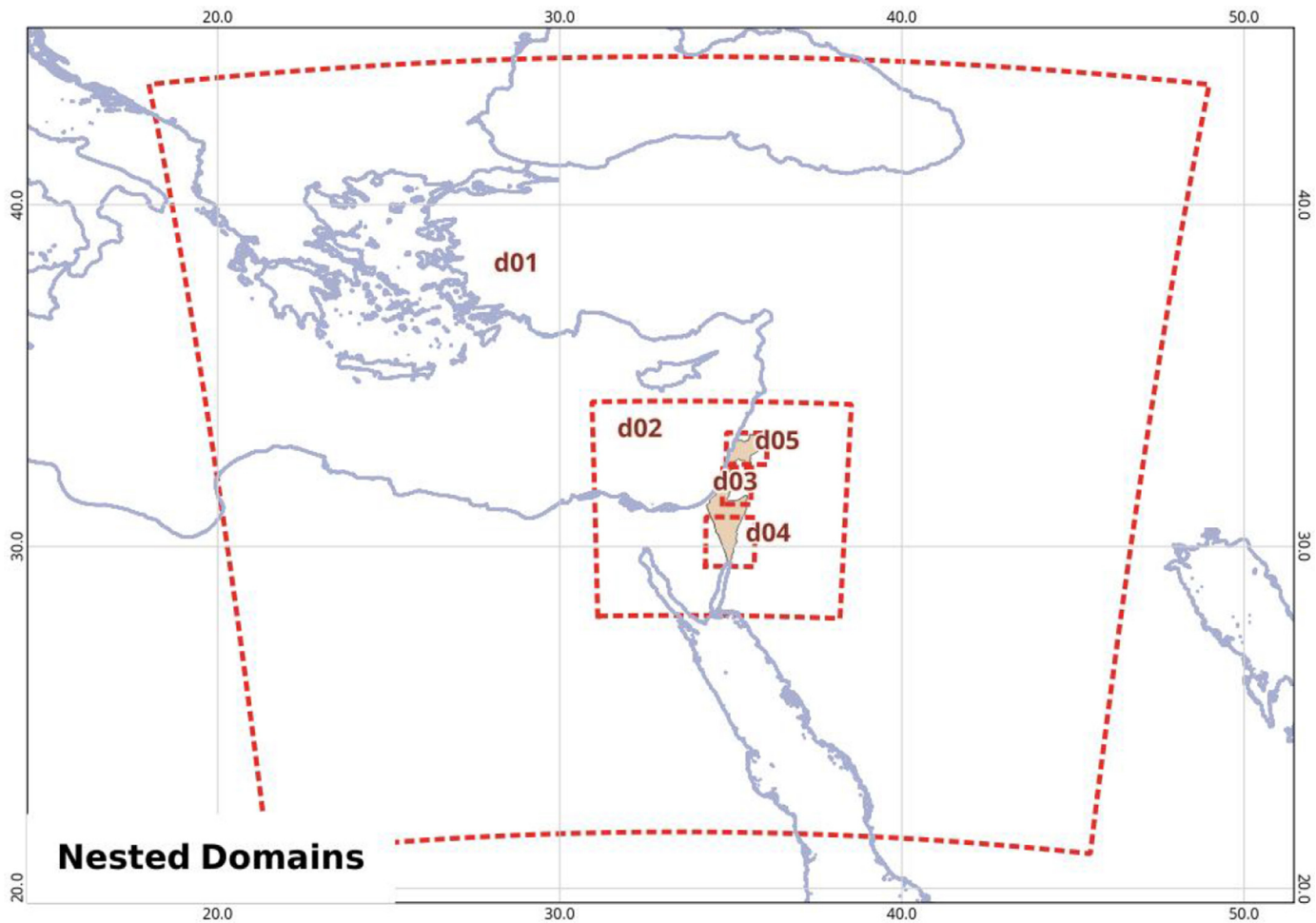


**Fig. 7.** All five domains: the outer has 13.5 km pixel size. The second has 4.5 km pixels and all three nested inner domains are at 1.5 km pixel size.

### 2.7.2. High resolution hydrological data

The key input dataset to WRF-Hydro that enables the model to merge climate parameters with the land surface is the high resolution terrain routing data. The SRTM elevation data served as the base on which these high resolution topographic and hydrological layers were built. A NetCDF file was prepared in the Lambert Conformal Conic (LCC) Coordinate Reference System (CRS) of the geogrid, geo\_em.d03.nc, but at a much finer resolution than the geogrid. Compared to the resolution of the inner domain d03 described above (Section 2.7.1) this hydrology dataset resolves at pixels 50 times finer than the geogrid. The dataset also contains point locations of the basin outlets. The model uses these basin drainage points to forecast runoff in the final output text file frst\_pts\_out.txt.

### 2.7.3. Observed runoff

The IHS maintains hydrometric stations at many basin outlets across the country that record the depth of flow during flood events. The flow depth records are transformed to flow rates using known tables of depth vs. flow rates, since the hydrometric stations are positioned in drainage channels with well defined cross sections. We obtained these flow rates from IHS for the basins under investigation. The locations of the hydrometric stations also appear in the model's high resolution land surface input data as forecast

points. Each actual hydrometric station is reflected within the model as a forecast point. Therefore we have a database of observed flow rates at the model's forecast points. This table of hourly observed discharges was compared to the model forecasts at the same outlet locations, and over parallel time spans.

### 2.7.4. Download of GFS climate data

From the GFS data archive website at <http://nomads.ncdc.noaa.gov/data/gfs4/> (Rutledge et al., 2005) files were downloaded for each of the storm events. We selected a uniform initialization time of 00Z (00:00 UTC) at approximately one to two days before the start of each storm and chose GFS data at 0.25° resolution. We acquired grib2 data files 144 h or 6 days from initialization, thus insuring that the full storm event was covered by the GFS climate forecasts.

The above GFS site maintains online data at the chosen resolution only for the previous 24 months. Originally two earlier storm events for two basins were to be examined: Uba during January 2013, and Zihor which flooded in January 2010. Both of these smaller basins are interesting in that they experience very high discharge rates but only once in several years. However meteorological forcing data for these early dates are available only through special order, and at the higher 0.5° resolution. Therefore the Uba and Zihor basins were eliminated.

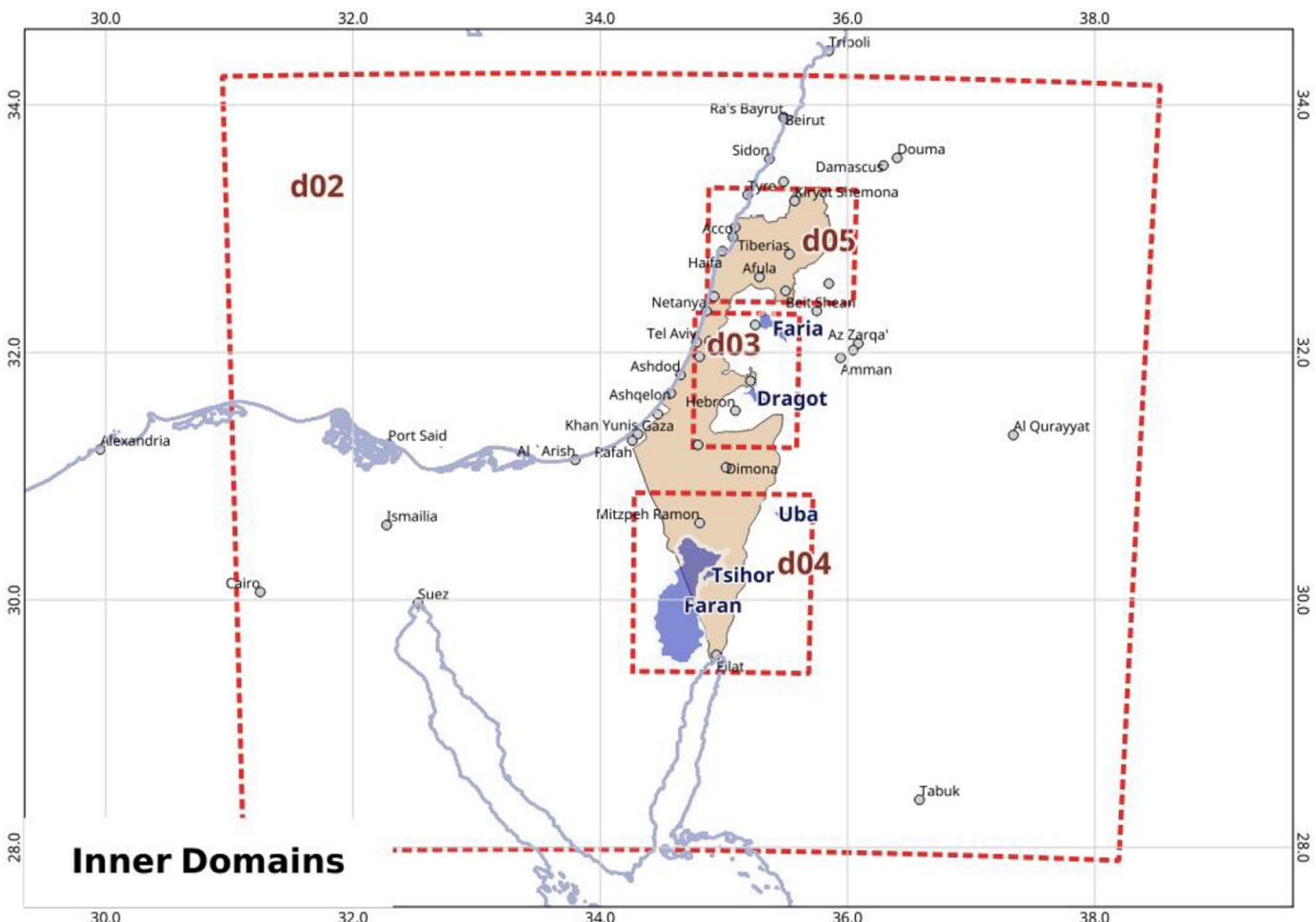


**Fig. 8.** Domain 3 covers the Faria and Dragot basins. Domain 4 covers Faran and Zihor as well as Uba.

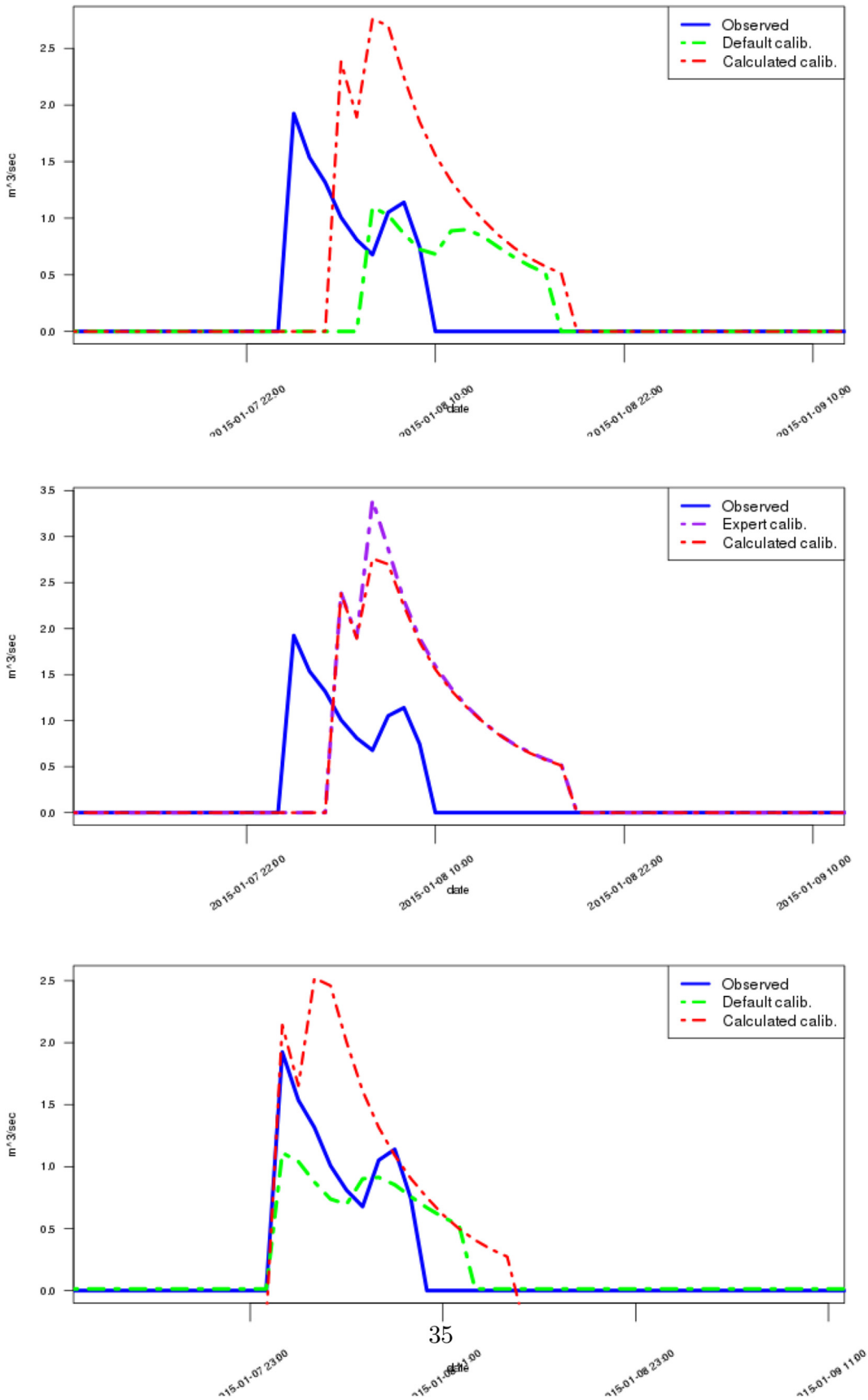


**Fig. 9.** Hydrographs from Darga basin, storm event of Jan, 2015. The default calibration somewhat under-predicts the peak runoff. The second graph shows curves that result from the expert calibration, displaying a higher peak than the observed. The third graph is shifted by the calculated time lag.

### 3. Results and discussion

#### 3.1. Results

##### 3.1.1. Hydrographs

Figs. 9 through 14 present hydrographs for the basins and storm events analyzed in this work. In each case the blue curve represents observed flow rates from hydrometric stations located at the basin outlets. The green and red dashed lines show predicted hydrographs from WRF-Hydro outputs using the default and calculated calibrations respectively.

For certain storm event, two or three graphs appear: the original forecasted flow rates (observed and two forecasts); flow rates as predicted by an expert calibration, colored purple; and time-shifted and rescaled graphs (see Section 3.2.1) which allow focusing on the match in shape between the hydrographs.

##### 3.1.2. Exploratory statistics

In an attempt to quantify the match between the observed and each predicted hydrograph, three comparative statistics were calculated. The Nash Sutcliffe Efficiency Index (NSE) is widely accepted as a measure of goodness of fit between model simulations and observed hydrographs. The value of NSE as a measure of the quality of hydrological forecasts has been re-examined (McCuen et al., 2006; Jain and Sudheer, 2008) and is still the accepted norm for evaluating model predictions.

The mean and standard deviation for each distribution of discharge flow rates individually were also examined. In addition we calculated the total discharge for each flood event, again for the observed and forecasted hydrographs. Total runoff, the area under the hydrograph curve, offers an additional indication of similarity between a forecast and the actual flood.

Tables 8–11 of these exploratory statistics show cases where mean flow of the prediction deviates from the observed. Nevertheless, comparing total runoff and NSE values of the default configurations to the calculated configurations reveals the quality of the calibration. It should be noted that the main source of error in flood forecasting is uncertainty in the climate input data. The uncertainty associated with precipitation forecasting is described by

Fiori et al. (2014), Hong and Lee (2009) and HAMILL, Thomas M. (2014). In this work, which covers "normal" flood events with two to ten year return periods, there is no expectation of a close match between the predicted and measured hydrographs. Rather we present NSE and other statistics as a relative comparison between different calibrations.

#### 3.2. Discussion

The distributions of flow rates are analyzed with the results from the default and calculated calibrations appearing in Tables 9 and 10. Statistics from the simulation using an expert calibration are presented in 11. The tables include the mean flow rate, total discharge and NSE for each basin/storm event combination.

##### 3.2.1. Timing of the hydrographs

In light of the goal of this research, presenting a method to determine three specific hydrological calibration parameters, we need to take into account and compensate for other factors. The inherent uncertainty in timing of climate forecasts (for example Strobach and Bel (2015) or Fiori et al. (2014)) necessarily causes a parallel uncertainty in hydrological forecasts, even before the slope and soil calibrations take effect. To compensate for this timing uncertainty, due mostly to the climate forecast, two statistical functions shift and recalculate the predicted flow rates.

First a cross correlation with time lag was calculated for each of the two observed/predicted pairs of flow rate data. In this technique, the cross correlation between the two distributions is calculated, while applying a time shift in hourly intervals for several hours before and after the original time. The time lag with the maximum cross correlation represents the optimal match in timing between the two distributions. Additionally, in order to focus on the shape of the hydrograph curves, the mean of the predicted values was rescaled to match the mean of the observed runoff. This rescaling helps to account for further uncertainty in the original climate data regarding the intensity of the storm event.

##### 3.2.2. Expert calibration

In a few cases, model forecasts which result from an expert

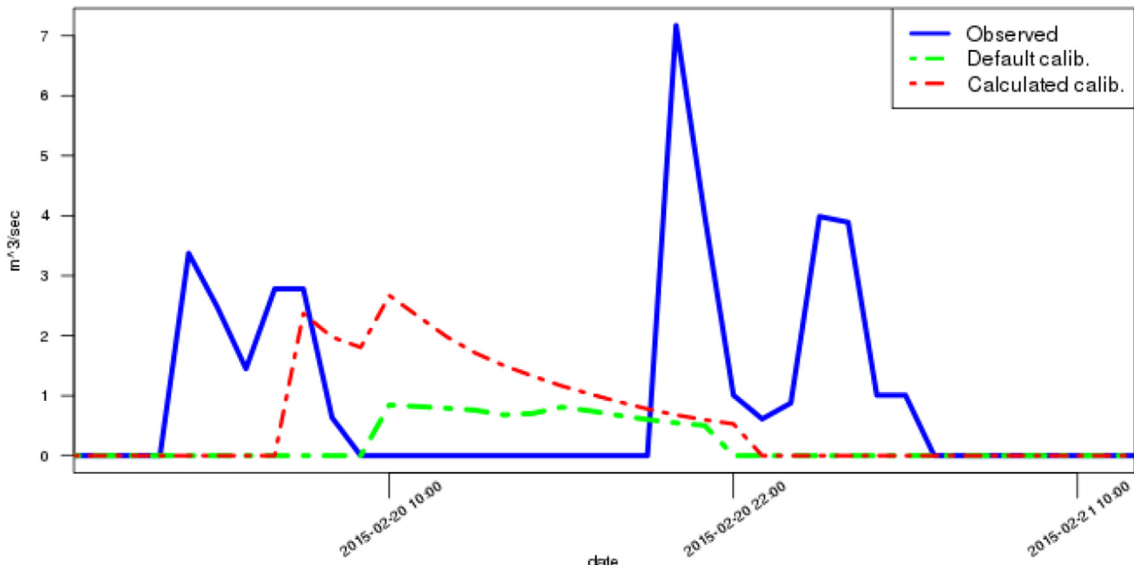


**Fig. 10.** Hydrographs from Darga basin, storm event of Feb, 2015. The calculated calibration shows a good match to the first discharge peak, while the default under estimates the discharge.

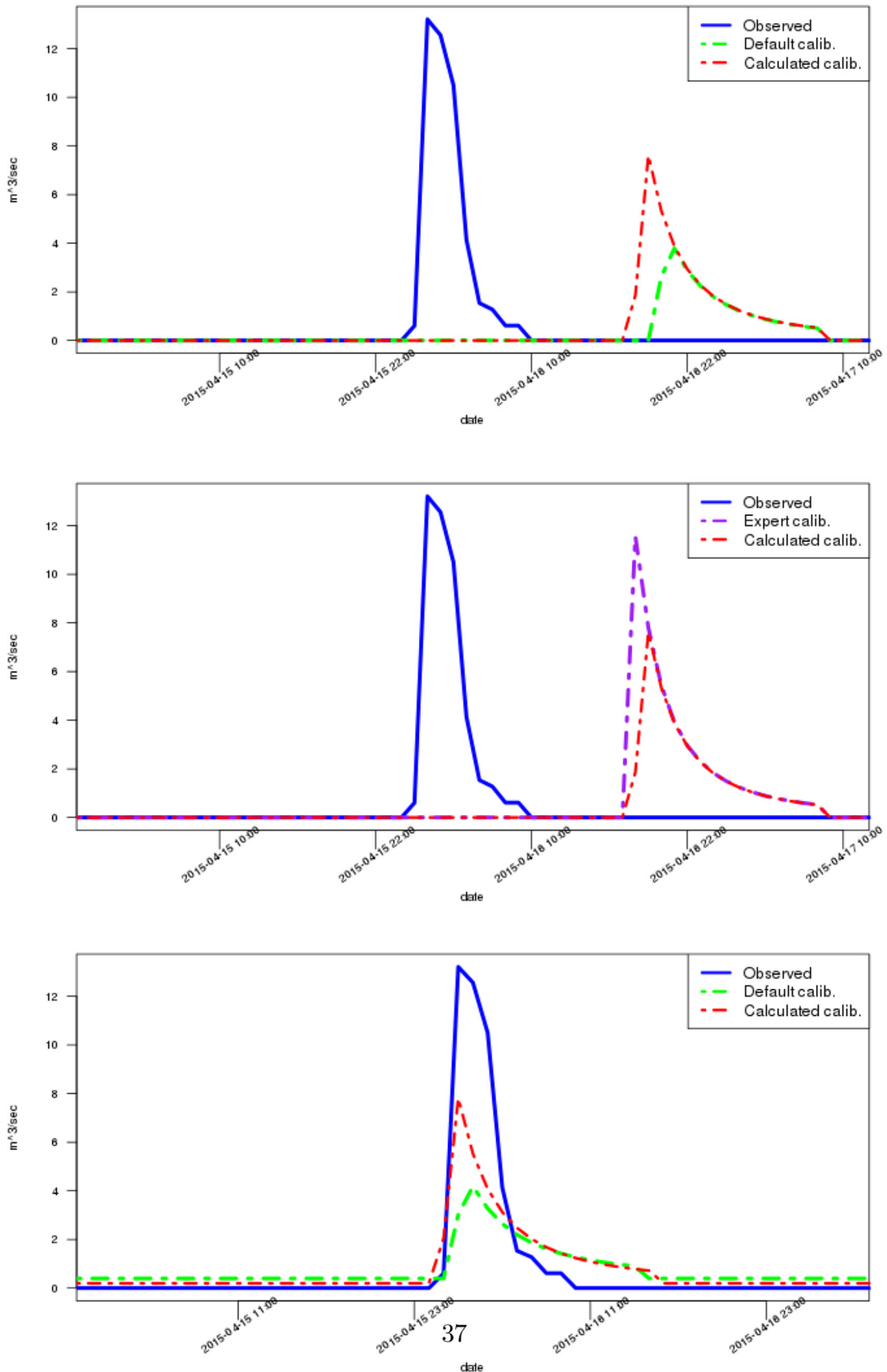


**Fig. 11.** Hydrographs from *Darga* basin, storm event of Apr, 2015. The calculated calibration in the first graph achieves a slightly better match. The second graph represents the forecast by produced by the expert calibration, showing a better match to the observed. The third graph shows the forecasts after the time lag shift.

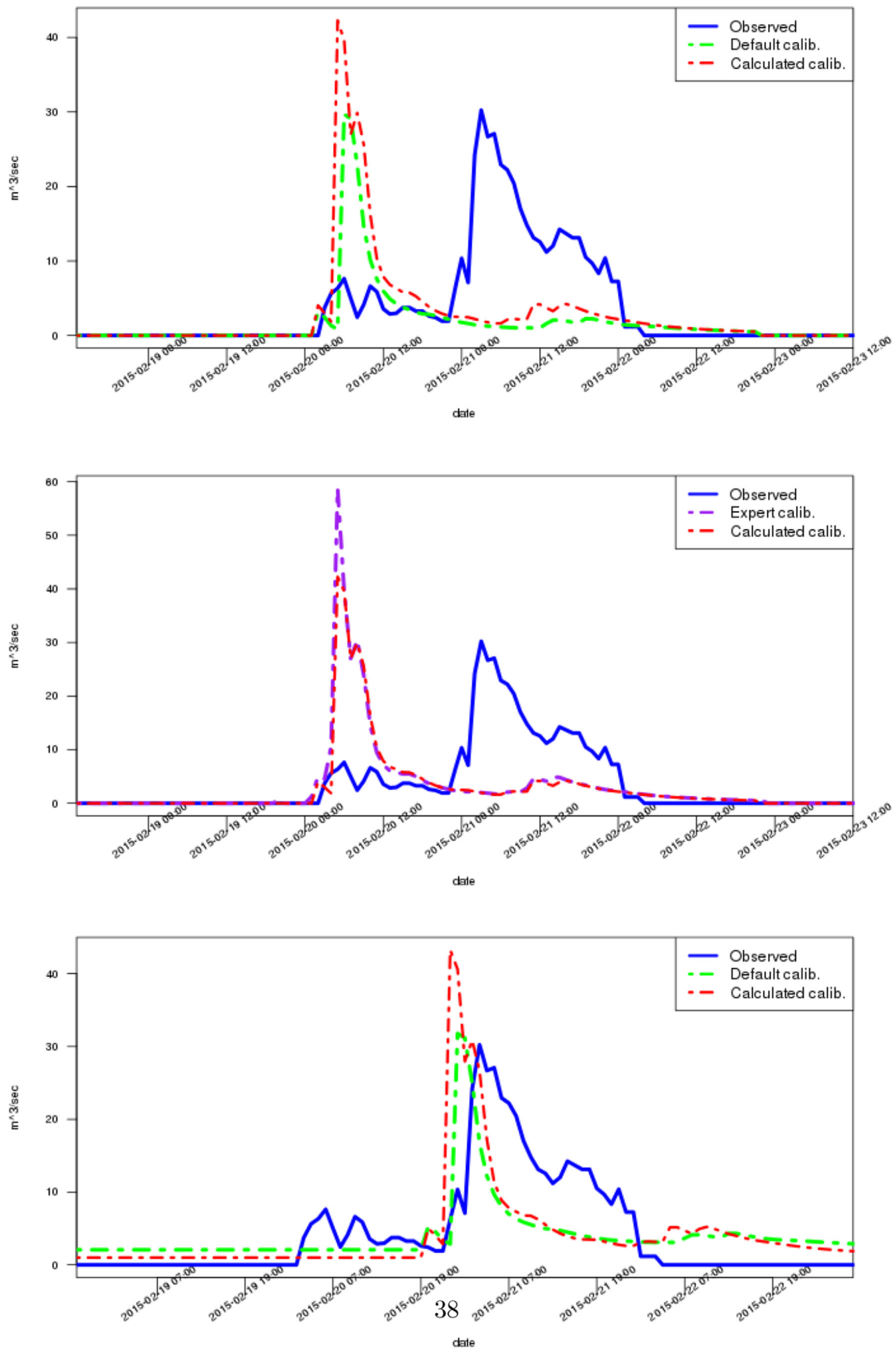


**Fig. 12.** Hydrographs from Arugot basin, storm event of Feb, 2015. In this simulation the calculated calibration again gives better results than the default. The second graph shows that the runoff hydrograph using an expert calibration overshoots the peak discharge. The third graph displays the time lag shift.

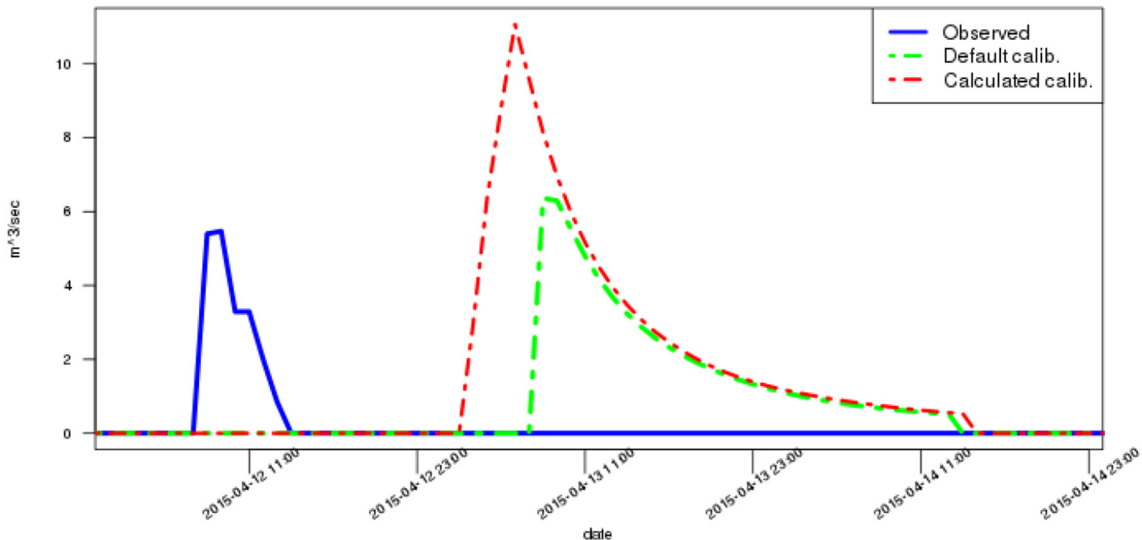


**Fig. 13.** Hydrographs from Arugot basin, storm event of Apr, 2015. Both forecasts show exaggerated discharges.

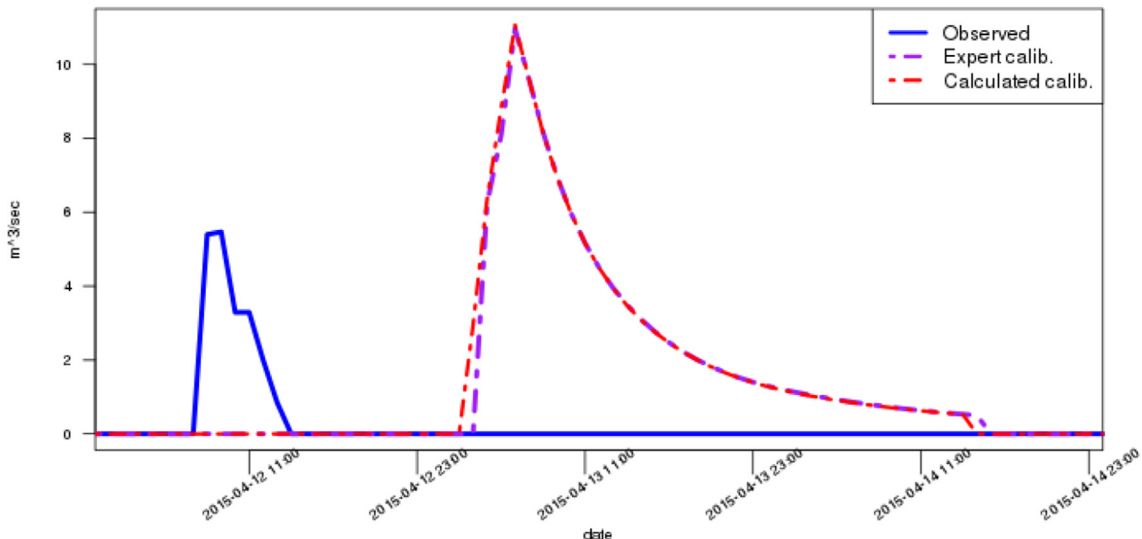


**Fig. 14.** These hydrographs show the expert calibration compared to the calculated calibration. Again both forecasts equally over predicted the flood.

**Table 8**  
Exploratory statistics of observed runoff.

Storm event Basin/Date	Mean flow $m^3/sec$	STD	Total disch $1000m^3$
Arugot Feb 2015	4.89	7.25	1689
Arugot Apr 2015	0.209	0.919	73
Darga Jan 2015	0.204	0.47	37
Darga Feb 2015	0.597	1.38	133
Darga Apr 2015	0.524	2.28	162

calibration are presented. The IHS constructed and tested various calibrations in the context of operational flood forecasting during the 2013–2015 seasons. Those parameters are implemented in an additional LSM calibration file, and applied to certain storm events. We show that the calculated calibration created in the context of this work achieves forecast results at least as good as the expert based calibration (i.e. Darga, Jan 2015 9 and Arugot Feb 2015 12).

**Table 9**  
Statistics of default calibration.

Storm event Basin/Date	Mean flow $m^3/sec$	STD	Total disch $1000m^3$	Lag hrs	NSE	NSE (Shifted)
Arugot Feb15	2.29	5.06	792	18	-0.512	-0.505
Arugot Apr15	0.65	1.46	227	14	-2.79	-2.84
Darga Jan15	0.19	0.355	34	-5	-0.303	-0.224
Darga Feb15	0.137	0.287	30	10	-0.142	-0.189
Darga Apr15	0.237	0.765	73	-18	-0.155	-0.172

### 3.2.3. Analysis of storm events

**3.2.3.1. Darga Jan, 2015.** During the early January, 2015 storm rain fell throughout the country, and brought snow to the northern mountains. The Israel Meteorological Service reports (<http://www.ims.gov.il/IMS/CLIMATE/ClimateSummary/>) that Arad in the eastern Negev received 174% of the annual average precipitation for the month of January.

**Table 10**

Statistics of calculated calibration.

Storm event	Mean flow	STD	Total disch	Lag	NSE	NSE
Basin/Date	$m^3/sec$		$1000m^3$	hrs		(Shifted)
Arugot Feb 15	3.64	7.56	1259	18	-0.872	-0.403
Arugot Apr 15	1.12	0.998	390	-18	-7.69	-0.534
Darga Jan 15	0.443	0.808	80	-3	-1.69	-0.389
Darga Feb 15	0.376	0.732	84	13	-0.276	0.181
Darga Apr 15	0.383	1.3	118	-17	-0.346	0.415

**Table 11**

Statistics of expert calibration.

Storm event	Mean flow	STD	Total disch	Lag	NSE	NSE
Basin/Date	$m^3/sec$		$1000m^3$	hrs		(Shifted)
Arugot Feb 15	3.93	8.53	1360	18	-1.13	-1.16
Arugot Apr 15	1.09	1	379	-18	-7.41	-5.59
Darga Jan 15	0.464	0.866	84	-3	-2.08	-1.69
Darga Feb 15	0.457	0.828	102	14	-0.249	-0.208
Darga Apr 15	0.501	1.87	155	-16	-0.652	-0.676

The hydrographs (9) show a fair, but somewhat exaggerated match between the observed and the forecasted runoff, while the default calibration under predicts discharge. The middle graph

overlays the expert forecast result with the calculated, showing that the expert forecast exaggerates the peak even more. In Tables 10 and 11 the expert forecast has lower (poorer) NSE values and somewhat higher total discharge than the calculated, pointing to good performance for the calculated parameters.

**3.2.3.2. Darga Feb, 2015 and Arugot Feb 2015.** February, 2015 also brought higher than annual average rainfall to the Dead Sea area. Neither of the forecasted hydrographs in the Darga basin caught the two separate peak flows, but the total discharge from the default was well below the actual total, whereas the calculated calibration was much closer to the observed (again in Tables 10 and 11). The lag-shifted forecast using the calculated calibration gave higher NSE than both the default and the expert calibrations. The expert calibration, on the other hand, showed total runoff closer to the observed value.

Examining the results for Arugot during this storm shows again a slight advantage to our calculated calibration. The NSE value is higher than the default and expert calibrations. Total discharge for this flood event was well predicted by both the calculated and expert, whereas the default under predicted by 50%. We present both the original graphs and the time shifted data (third graph in Fig. 12), prepared using the cross covariance with time lag procedure. This demonstrates the fit of the predicted hydrographs when timing uncertainty in the climate data is canceled out. As explained (3.2.1), while none of the forecasts correctly predicted

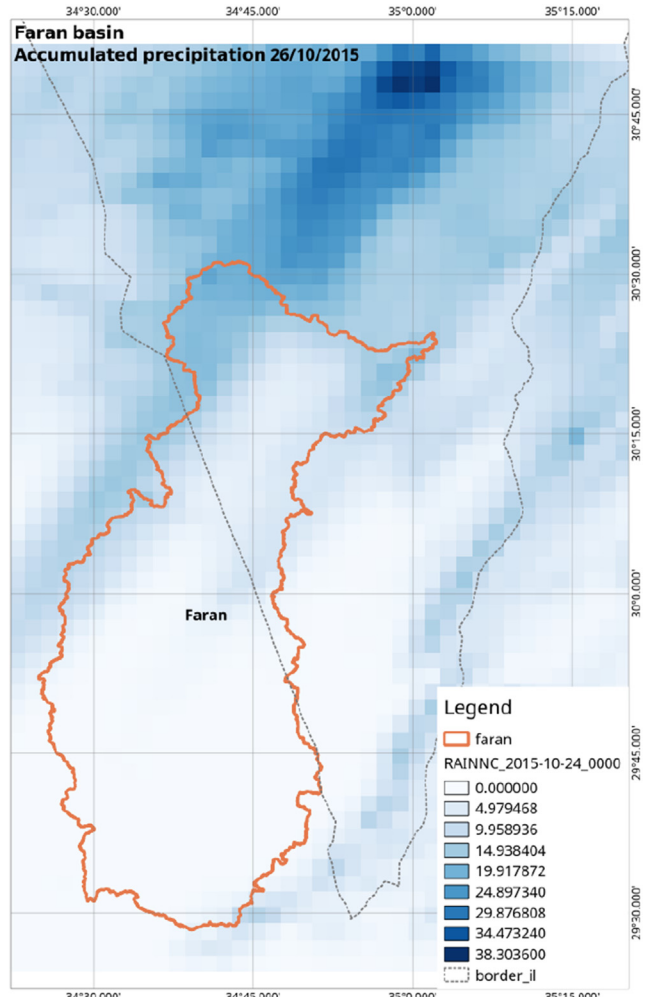
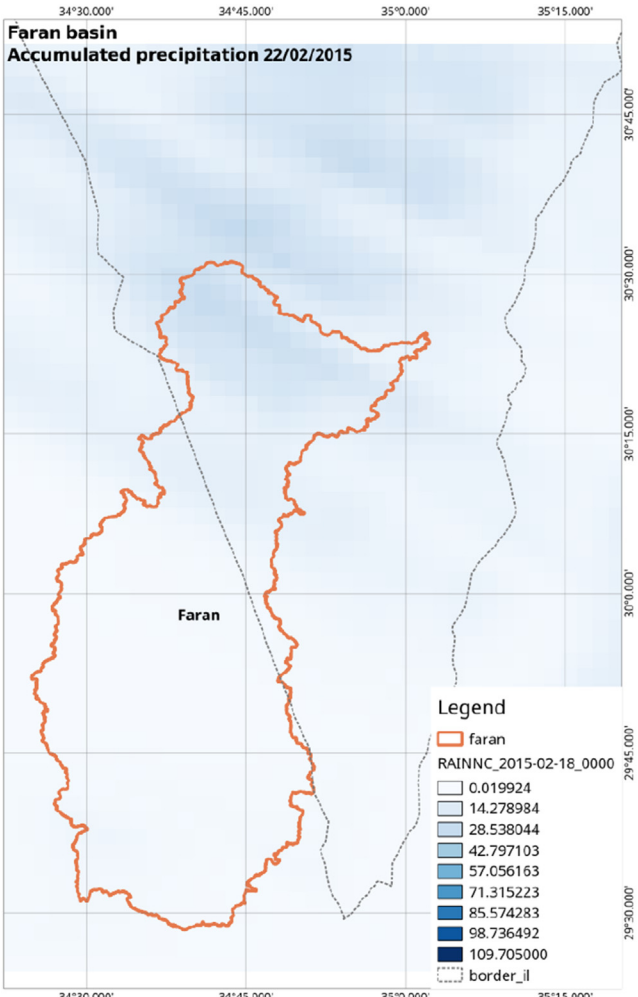


**Fig. 15.** Accumulated precipitation in the Faran basin, storm events of Oct, 2015 and Feb 2015.

this storm event, we focus only on the comparative closeness of fit between the calibrations, and not the absolute closeness of fit to observed data.

**3.2.3.3. Darga Apr 2015 and Arugot Apr, 2015.** The April 2015 results in Darga show explicitly that the calculated calibration proves better than the simulation with default calibration. NSE values are better than both the default and the expert calibrations. While both forecasts undershoot the actual peak, the default is much weaker. But we also point out that the expert calibration reached a value of total runoff much closer to the actual measured runoff than both other forecasts.

The IMS report for this event focuses on heavy rain and snow in the northern mountains but only a minimal 6–7 mm along the Dead Sea and Sodom region. The flood in the Arugot basin during this event was over-estimated by both calibrations. We note that the peak flow rate was very small, probably leading to the poor results in both cases. Fig. 14 shows both our calculated calibration and the expert calibration compared to observed runoff. In both cases the forecasts exaggerated the peak and total runoffs, but the calculated and expert curves closely overlap, leading to the possible conclusion that the initial climate data, and not hydrological parameters caused this miss in forecast.

**3.2.3.4. Faran Mar, 2014.** We examined three storm events in the Faran basin: October 2015, February 2015 and March 2014. None of these flood events appeared in the simulation outputs. Recognizing that the Faran basin covers approximately 3000 square kilometers, we postulate that only large storm events (in relation to the basin size) with high runoff are resolved by the model. The observed runoff rate in this event of  $30 \text{ m}^3/\text{sec}$  has a once in two year (50%) probability, according to a table published<sup>6</sup> by the IHS. Thus for such a large basin this flow rate is very small, causing the model to miss the runoff entirely.

#### 3.2.4. Events missed by the model

In the course of inspecting the model simulation results, a few flood events did not appear at all in the WRF-Hydro output files. Observed runoff in the Faran basin on February 21, 2015 peaked at  $42 \text{ m}^3/\text{sec}$ , and in Darga on November 21, 2014 the IHS hydrometric station recorded a peak of  $11 \text{ m}^3/\text{sec}$ . Yet these events, as well as the October 26, 2015 flood in Faran were missed by the model.

While this work focuses on hydrological parameters, it is worthwhile examining the rain forecasts to verify whether the WRF model actually predicted rainfall. If the climate component of the model under-predicts precipitation rates, the hydrological component cannot forecast runoff. We extract the RAINNC variable from the WRF output, which represents accumulated precipitation, for the February 2015 and October 2015 storms. These forecasted total precipitation maps, overlaid with the basin perimeter, are shown in Fig. 15. Clearly the WRF hydro-meteorological data, which serves as input to WRF-Hydro, predicted only a few millimeters of rain throughout the basin during these events. Therefore we conclude that the lack of predicted runoff from WRF-Hydro results, most likely, from uncertainty in the original GFS meteorological data, carried on to the WRF rain predictions.

## 4. Conclusions

### 4.1. Summary

This work presents a procedure, based on soil texture and

topography, for constructing a set of WRF-Hydro calibration files. We employ remote sensing, GIS methods, published tables of saturated hydraulic conductivity, and rain/runoff measurements to obtain reasonable approximations for three parameters: REFDK, REFKDT, and SLOPECAT. This approach paves the way to rapidly deduce other hydrological parameters employed by WRF-Hydro such as surface roughness and soil retention depth.

Model simulation runs on seven storm events over that past two years show evidence that our prepared calibration forecast reveals a closer match to observed runoff than the forecast obtained with a default setup. We additionally demonstrate that our calibration fares well against an expert based calibration over the same storm events. The match with observed runoff data is examined both visually, in runoff hydrographs and with two statistics: total discharge and the Nash-Sutcliffe Index.

From those events that were missed by the model, we suggest two short-comings of WRF-Hydro: the flow rate needs be significant in relation to the size of the basin; and the model is not able to resolve events with a very short time scale.

### 4.2. Future research

This research on calibration of the WRF-Hydro model has exposed several possible directions for future work.

- Expanding the concepts in this work to other hydrological parameters should be first priority. While the specifics of methodology will change, the remote sensing approach and bypassing repeated trial-and-error calibration runs shows further promise.
- We state (Section 2.2.4) that determining soil parameters from satellite imagery cannot work in forested or agricultural areas. However the lithology data, supplied by the Geographic Survey of Israel, also covers forests and agricultural fields. Would patching the derived soil hydraulic parameters to the lithology layer for these forested areas improve the forecasts in those basins?
- In estimating the REFKDT parameter, we adopt soil parameters from some field experiments (Section 2.5) and used the SWB equation to solve for  $K_{dt}$ . This approach requires additional work in matching field experiments to forecasted runoff for specific soil types.
- We suggest some limitations of WRF-Hydro insofar as size and time spread of flow in a basin. This hypothesis deserves additional attention.

### Acknowledgements

I would like to express appreciation to the Israeli Hydrological Service and in particular to Dr. Amir Givati for supplying model simulation data and for sharing his experience in calibrating the WRF-Hydro model. Funding for this research from Karlsruhe Institute of Technology IMV-IFU under the "Integrating Microwave Link Data For Analysis of Precipitation" (IMAP) grant (DFG grant number: GZ: KU2090/7-2, AOBJ: 633213) was obtained in collaboration with IHS. Dr. Ran Kalvo from the Geological Survey of Israel also assisted by supplying soil lithology data layers.

Thomas Rummel, from the University of Augsburg willing shared his experience and computer code to advance this work. Dave Gochis from NCAR gave his valuable support and encouragement.

I am additionally grateful to the Arava Drainage Authority and Gil Slevin for allowing me time to take part in this research. Ami Shaham, Gil's predecessor as manager of the Arava Drainage Authority, deserves special mention since he initiated the use of GIS in

<sup>6</sup> <http://floods.online/home/Probability> in hebrew.

the Arava 15 years ago and gave me the opportunity to delve into the subject.

## 5. Appendix: Procedures and scripts

### 5.1. Software Availability

Four main software applications served to perform the procedures presented in this work.

- **GRASS-GIS**, an open source program [GRASS Development Team \(2015\)](#) available for multiple computer architectures from: <https://grass.osgeo.org/download/>.
- The **R Project** for Statistical Computing. This open source statistics software can also be downloaded for multiple computing platforms from <https://www.r-project.org/>.
- **ArcGIS**<sup>®</sup> was used to produce the high resolution terrain routing grid.
- The Nash-Sutcliffe Efficiency Index is implemented in a wide variety of software. We used the **Matlab**<sup>®</sup> function in this work. Matlab was also employed to solve and plot the SWB equation using the optimization function fminbound () .

The scripts developed in the course of this research will be made available on request from the corresponding authors.

### 5.2. Scripts

#### High Resolution Terrain Routing Grid

We employed a tool running in ArcGIS ([Sampson and Gochis, 2014](#)) to produce the terrain routing grid.

#### Atmospheric Correction

The GRASS GIS procedure for performing atmospheric correction of Landsat 8 image bands reads a set of parameters for 6S. Files were written for each of the three Landsat tiles, and each of the bands. The lines for water vapor, aerosol optical depth and Landsat band changed from file to file. The module i.atcorr reads the Landsat metadata file and also accepts a digital elevation model as input to correct for topography height above sea level.

#### Classification of Landsat Bands

The GRASS GIS script for creating a classified raster layer of soil types draws on the SMAP algorithm. First a reflectance signature file is built using the i.gensigset module, then i.smap is called to perform the classification, producing from the original six Landsat bands, a soil classification raster. This raster is reclassed to the four soil types chosen in this work.

#### Preparing SLOPECAT calibration data

The GRASS GIS commands used to prepare the SLOPECAT calibration include r.slope.aspect to prepare the initial slope raster. Coordinate reference system settings and resolution are manipulated in the usual way. Then the r.resamp.stats module allows for aggregating the fine resolution slope class rasters to the coarse (domain) resolution required for the calibration file. The r.out.gdal module exports the GRASS raster directly to NetCDF format, and NCO commands such as ncldump, ncap2 and ncatted are used to read attributes and write variables to the LSM calibration file.

#### Preparing REFKDT and REFKDT calibration data

After the classification step, soil classes are re-classed twice according to value of  $K_{sat}$  (in units of  $10^{-6}$  m/sec) and REFKDT values according to [Table 5](#) for each soil type, resulting in the two new rasters. The reclass step is performed after switching to the

Lambert Conformal Conic coordinate reference system employed in our simulation. Additionally, resolution and extents are read from the LSM file and these values used to determine the resolution for the WRF inner domain. Finally, both of the rasters are exported as NetCDF files and merged into our calibrated LSM.

Within the script, GRASS modules r.reclass and r.mapcalc manipulate the rasters. Then the same commands used to export the SLOPECAT and merge into the LSM calibration file are employed again here.

#### Collating Irregular Discharge Data

The script, written in R, calls the package zoo to collect discharge readings at irregular times, and to create average hourly discharges over the whole time period of the original data. First a CSV file of the irregularly spaced discharge data is read in and converted to a zoo dataset. Readings that are closer than 1 h are averaged together. An empty table of hourly intervals is created, and the above averages are associated with the correct time slot. Then using the na.locf function, missing time slots are filled.

#### Nash-Sutcliffe Efficiency index

This statistic is calculated by:

$$E_f = 1 - \frac{\sum_{t=1}^n [\hat{D}_t - D_t]^2}{\sum_{t=1}^n [D_t - \bar{D}]^2} \quad (9)$$

where  $\hat{D}_t$  is the observed runoff,  $D_t$  is the modeled runoff, both at time  $t$ , and  $\bar{D}$  is the mean observed runoff. The fraction in equation (9) is essentially the sum of squares of the difference between observed data and the prediction, divided by the covariance of the observed data. By subtracting this fraction from unity, NSE values close to 1 indicate a very good fit, while values below 0 show poor matches.

## References

- Akbar, M., Aliabadi, S., Patel, R., Watts, M., 2013. A fully automated and integrated multi-scale forecasting scheme for emergency preparedness. Environ. Model. Softw. 39, 24–38. <http://dx.doi.org/10.1016/j.envsoft.2011.12.006>. <http://linkinghub.elsevier.com/retrieve/pii/S136481521100301X>.
- Arnault, J., Wagner, S., Rummel, T., Fersch, B., Bleifernicht, J., Andersen, S., Kunstmann, H., 2015, <http://dx.doi.org/10.1175/JHM-D-15-0089.1>. Role of runoff-infiltration partitioning and resolved overland flow on land-atmosphere feedbacks. J. Hydrometeorol.
- Biondi, D., De Luca, D.L., 2015. Process-based design flood estimation in ungauged basins by conditioning model parameters on regional hydrological signatures. Nat. Hazards 79, 1015–1038. <http://dx.doi.org/10.1007/s11069-015-1889-1>.
- Chen, F., Dudhia, J., 2001. Coupling an Advanced Land Surface Hydrology Model with the Penn State–NCAR MM5 Modeling System. MONTHLY WEATHER REVIEW 129.
- Chen, F., Manning, K., Barlage, M., Gochis, D., Tewari, M., 2008. NCAR High-resolution Land Data Assimilation System and its Recent Applications.
- Chen, Y., Li, J., Xu, H., 2016. Improving flood forecasting capability of physically based distributed hydrological models by parameter optimization. Hydrology Earth Syst. Sci. 20, 375–392. <http://dx.doi.org/10.5194/hess-20-375-2016>.
- Dan, J., Yaalon, D., Moshe, R., Nissim, S., 1982. Evolution of reg soils in southern Israel and sinai. Geoderma 28, 173–202.
- Duan, Q., Sorooshian, S., Gupta, V., 1994. Optimal use of the SCE-UA global optimization method for calibrating watershed models. J. Hydrology 265–284.
- Fiori, E., Cornellas, A., Molini, L., Rebora, N., Siccaldi, F., Gochis, D., Tanelli, S., Parodi, A., 2014. Analysis and hindcast simulations of an extreme rainfall event in the Mediterranean area: the Genoa 2011 case. Atmos. Res. 138, 13–29. <http://dx.doi.org/10.1016/j.atmosres.2013.10.007>.
- Foody, G.M., Ghoneim, E.M., Arnell, N.W., 2004. Predicting locations sensitive to flash flooding in an arid environment. J. Hydrology 292, 48–58. <http://dx.doi.org/10.1016/j.jhydrol.2003.12.045>.
- Fredj, E., Silver, M., Givati, A., 2015. An integrated simulation and distribution system for early flood warning. Water Resour. Manag. 4 (3).
- Gallagher, M., Doherty, J., 2007. Parameter estimation and uncertainty analysis for a watershed model. Environ. Model. Softw. 22, 1000–1020. <http://dx.doi.org/10.1016/j.envsoft.2006.06.007>.
- Garcia, S.G., 2004. GRASS GIS-embedded Decision support framework for flood

- simulation and forecasting. *Trans. GIS* 8, 245–254. [http://www.spatial.redlands.edu/sds/downloads/Garcia2004\\_GRASSGISEmbeddedDecisionSupportFrameworkForFloodSimulationAndForecasting.pdf](http://www.spatial.redlands.edu/sds/downloads/Garcia2004_GRASSGISEmbeddedDecisionSupportFrameworkForFloodSimulationAndForecasting.pdf).
- Gebbert, S., Pebesma, E., 2014. A temporal GIS for field based environmental modeling. *Environ. Model. Softw.* 53, 1–12. <http://www.sciencedirect.com/science/article/pii/S136481521300282X>.
- Gheith, H., Sultan, M., 2002. Construction of a hydrologic model for estimating Wadi runoff and groundwater recharge in the Eastern Desert, Egypt. *J. Hydrology* 263, 36–55.
- Givati, A., Lynn, B., Liu, Y., Rimmer, A., 2012. Using the WRF model in an operational streamflow forecast system for the Jordan river. *J. Appl. Meteorology Climatol.* 51, 285–299. <http://dx.doi.org/10.1175/JAMC-D-11-082.1>.
- Gochis, D., Yu, W., Yates, D., 2013. NCAR WRF-hydro Technical Description and User Guide. [http://www.ral.ucar.edu/projects/wrf\\_hydro/images/WRF\\_Hydro\\_Technical\\_Description\\_and\\_User\\_Guide\\_v1.0.pdf](http://www.ral.ucar.edu/projects/wrf_hydro/images/WRF_Hydro_Technical_Description_and_User_Guide_v1.0.pdf).
- Goncalves, M.C., Pereira, L.S., Leij, F.J., 2008. Pedo-transfer functions for estimating unsaturated hydraulic properties of Portuguese soils. *Eur. J. Soil Sci.* 48, 387–400. <http://dx.doi.org/10.1111/j.1365-2389.1997.tb00205.x>.
- GRASS Development Team, 2015. Geographic Resources Analysis Support System (GRASS GIS) Software. Open Source Geospatial Foundation, USA. <http://grass.osgeo.org>.
- Greenbaum, N., Salmon, O., Schick, A., 2003. Geomorphological implications and hydrological applications of infiltration tests in a hyperarid region. *Horizons Geogr.* 57, 44–69.
- Grohmann, C.H., Riccomini, C., Chamani, M.A.C., 2011. Regional scale analysis of landform configuration with base-level (isobase) maps. *Hydrology Earth Syst. Sci.* 15, 1493–1504. <http://dx.doi.org/10.5194/hess-15-1493-2011>.
- HAMIL, Thomas M., 2014. Performance of Operational Model Precipitation Forecast Guidance during the 2013 Colorado Front-range Floods. Physical Sciences Division, NOAA/Earth System Research La. <http://dx.doi.org/10.1175/MWR-D-14-0007.1>.
- Hogue, T.S., Sorooshian, S., Gupta, H., Holz, A., Braatz, D., 2000. A multistep automatic calibration scheme for river forecasting models. *J. Hydrometeorol.* 1, 524–542.
- Hong, S.Y., Lee, J.W., 2009. Assessment of the WRF model in reproducing a flash-flood heavy rainfall event over Korea. *Atmos. Res.* 93, 818–831. <http://dx.doi.org/10.1016/j.atmosres.2009.03.015>.
- Jain, S.K., Sudheer, K., 2008. Fitting of hydrologic models: a close look at the NashSutcliffe index. *J. HYDROLOGIC Eng.* 13, 981–986. [http://dx.doi.org/10.1061/\(ASCE\)1084-0699\(2008\)13:10\(981\)](http://dx.doi.org/10.1061/(ASCE)1084-0699(2008)13:10(981)).
- Kumar, S.V., Peters-Lidard, C.D., Eastman, J.L., Tao, W.K., 2008. An integrated high-resolution hydrometeorological modeling testbed using LIS and WRF. *Environ. Model. Softw.* 23, 169–181. <http://dx.doi.org/10.1016/j.envsoft.2007.05.012>.
- McCauley, J.D., Engel, B., others, 1995. Comparison of scene segmentations: SMAP, ECHO, and maximum likelihood. *Geoscience and Remote Sensing, IEEE Trans.* 33, 1313–1316.
- McCuen, R.H., Knight, Z., Cutter, A., 2006. Evaluation of the NashSutcliffe efficiency index. *J. HYDROLOGIC Eng.* 11, 587–602. doi:10.1061/(ASCE)1084-0699(2006)11:6(597).
- Meiri, E., 2015. The Influence of Soil Surface Characteristics on Rain-runoff Ratios in an Extreme Arid Desert during Natural Precipitation. Masters. Hebrew University.
- Neteler, M., Bowman, M.H., Landa, M., Metz, M., 2012. GRASS GIS: a multi-purpose open source GIS. *Environ. Model. Softw.* 31, 124–130. <http://dx.doi.org/10.1016/j.envsoft.2011.11.014>.
- Nourani, V., Fard, A.F., Niazi, F., Gupta, H.V., Goodrich, D.C., Kamran, K.V., 2015. Implication of remotely sensed data to incorporate land cover effect into a linear reservoir-based rainfallrunoff model. *J. Hydrology* 529, 94–105. <http://dx.doi.org/10.1016/j.jhydrol.2015.07.020>.
- Ohana-Levi, N., Karnieli, A., Egozi, R., Givati, A., Peeters, A., 2015. Modeling the effects of and-cover change on rainfall-runoff relationships in a emirid, eastern Mediterranean watershed. *Adv. Meteorology* 2015. <http://dx.doi.org/10.1155/2015/838070>.
- Pennelly, C., Reuter, G., Flesch, T., 2014. Verification of the WRF model for simulating heavy precipitation in Alberta. *Atmos. Res.* 135–136, 172–192. <http://dx.doi.org/10.1016/j.atmosres.2013.09.004>.
- Raab, C., Barrett, B., Cawkwell, F., Green, S., 2015. Evaluation of multi-temporal and multi-sensor atmospheric correction strategies for land-cover accounting and monitoring in Ireland. *Remote Sens. Lett.* 6, 784–793. <http://dx.doi.org/10.1080/2150704X.2015.1076950>.
- Ramirez, E., Shuttle Radar Topography Mission. URL:<http://www2.jpl.nasa.gov/srtm/missionoverview.html>.
- (completely rev.) ed. In: Ritzema, H.P. (Ed.), 1994. *Drainage Principles and Applications*. Number 16 in ILRI Publication, 2. ed. ILRI, Wageningen.
- Rozenstein, O., Karnieli, A., 2011. Comparison of methods for land-use classification incorporating remote sensing and GIS inputs. *Appl. Geogr.* 31, 533–544. <http://dx.doi.org/10.1016/j.apgeog.2010.11.006>.
- Rutledge, G.K., Alpert, J., Ebuidaki, W., 2005. NOMADS: a Climate and Weather Model Archive at the National Oceanic and Atmospheric Administration. AMERICAN METEOROLOGICAL SOCIETY.
- Salvadore, E., Bronders, J., Batelaan, O., 2015. Hydrological modelling of urbanized catchments: a review and future directions. *J. Hydrology* 529, 62–81. <http://dx.doi.org/10.1016/j.jhydrol.2015.06.028>.
- Sampson, K., Gochis, D., 2014. WRF Hydro Routing Grid Pre-processor Python Toolbox Documentation, version2.0.
- Schaake, J.C., Koren, V.I., Duan, Q.Y., 1996. Simple water balance model for estimating runoff at different spatial and temporal scales. *J. Geophys. Res.* 101, 7461–7475.
- Schaap, M.G., Leij, F.J., van Genuchten, M.T., 2001. ROSETTA: a computer program for estimating soil hydraulic parameters with hierarchical pedotransfer functions. *J. hydrology* 251, 163–176.
- Strobach, E., Bel, G., 2015. Improvement of climate predictions and reduction of their uncertainties using learning algorithms. *Atmos. Chem. Phys. Discuss.* 15, 7707–7734. <http://dx.doi.org/10.5194/acpd-15-7707-2015>.
- Wosten, J., Pachepsky, Y., Rawls, W., 2001. Pedotransfer functions: bridging the gap between available basic soil data and missing soil hydraulic characteristics. *J. Hydrology* 251, 123–150.
- Yilmaz, K.K., Gupta, H.V., Wagener, T., 2008. A process-based diagnostic approach to model evaluation: application to the NWS distributed hydrologic model: PROCESS-BASED DIAGNOSTIC EVALUATION OF HYDROLOGIC MODEL. *Water Resour. Res.* 44 <http://dx.doi.org/10.1029/2007WR006716> n/a–n/a.
- Yucel, I., Onen, A., Yilmaz, K., Gochis, D., 2015. Calibration and evaluation of a flood forecasting system: utility of numerical weather prediction model, data assimilation and satellite-based rainfall. *J. Hydrology* 523, 49–66. <http://dx.doi.org/10.1016/j.jhydrol.2015.01.042>.
- Zobler, L., 1986. A World Soil File for Global Climate Modeling.